Dynamical Realisations and Numerical Diagnostics of an ECSM Cosmology

Adam Sheldrick

February 1, 2026

Abstract

This companion paper provides mechanistic clarification and supporting analysis for the superfluid medium framework introduced in "Unified ECSM Cosmology" (Paper 1). No new foundational postulates are introduced. Instead, we clarify the physical meaning of medium "flow" in the superfluid phase-field sense, address steady-state energy accounting, derive a transparent medium-based interpretation of inertia, and explain why local physics can exhibit effectively Lorentzian behavior despite an underlying medium. We also outline illustrative toy simulations demonstrating (i) extended, approximately flat rotation curves from baryon-coupled medium response and (ii) a baryonic Tully–Fisher-like scaling as a constraint on the coupling structure. Detailed cosmological redshift modeling and large-scale velocity-field reconstructions (e.g., Virgo infall) are deferred to subsequent work. This paper presents dynamical realizations and numerical diagnostics of ECSM cosmology. The purpose is not parameter fitting or data confrontation, but to demonstrate internal consistency, stability, and qualitative behavior of the governing equations. Observational comparison is deferred to companion papers.

Scope and relation to Paper I

This work serves as a technical companion to Paper I, providing explicit dynamical interpretations, supporting derivations, and illustrative simulations of the medium-based framework introduced there. No new fundamental assumptions are added. We focus on how the assumed ECSM dynamics give rise to energetically consistent steady configurations, inertia as resistance to medium reconfiguration, and effective local Lorentz symmetry in the low-energy regime. Phenomenological claims are limited to regimes already discussed in Paper I.

1 Introduction

Paper I introduced a unified cosmological framework in which gravitational, inertial, and cosmological phenomena emerge from the dynamics of a single superfluid-like medium. While that work focused on establishing internal consistency and broad observational viability, many of its claims invite a more explicit mechanistic treatment.

The purpose of the present work is to supply that missing layer. We provide concise physical interpretations and supporting analysis that clarify how (i) steady-state "gravitational" configurations can persist without dissipation or energy leakage, (ii) inertia can arise as resistance to the medium reconfiguration under acceleration, and (iii) local relativistic behavior can emerge effectively at low energies. We also include simple numerical diagnostics illustrating how baryon-coupled medium response can produce galaxy-scale regularities.

ECSM (Emergent Condensate Superfluid Medium) treats the vacuum as an effectively superfluid, condensate-like medium with dynamical fields whose gradients and defects carry

stress, transport, and energy. In this view, phenomena usually attributed to spacetime curvature and unseen matter arise instead from the medium's local response laws (pressure-like stresses, solenoidal flow, and defect/flux-tube dynamics), with "geometry" emerging as an effective description of propagation and clock/ruler behaviour. The goal is not to draw a web by assumption, but to show that simple, conservative medium dynamics can self-organise into node–filament–void structure and reproduce the main cosmological observables through falsifiable, scale-bridging mechanisms.

Interpretive Convention and Terminology

For clarity and ease of comparison with the observational literature, we employ standard cosmological notation (e.g. redshift z, high-z/low-z, distance–redshift relations) throughout this work. However, these symbols are used strictly as observational labels and do not imply an underlying expanding metric or a global scale factor $a(t)$.

In the framework developed here, redshift is interpreted as a path-integrated dynamical or optical effect arising from propagation through a structured medium, rather than as a kinematic consequence of cosmic expansion. Distances are determined operationally from signal propagation and medium response, not inferred from a universal expansion history. Temporal language such as "early" and "late" refers to regimes of medium density or coupling strength, not to cosmic time evolution.

A summary of correspondences is provided below:

Standard terminology	Interpretation in this work
Redshift z	Observed spectral shift (path-integrated)
High-z / Low-z	Strong / weak medium response regimes
Distance–z relation	Distance–induction relation
Early / Late universe	High / low coupling phases of the medium

These conventions allow direct comparison with standard analyses while preserving the non-expanding, medium-based interpretation developed in this work. Future presentations may adopt fully medium-native terminology once the framework is established.

1.1 Canonical definition of redshift in a state-dependent medium

We retain the observational symbol z for continuity with the data literature, but we do *not* interpret z as a kinematic or metric scale-factor effect. In this framework, redshift is an *optical response* accumulated along the photon trajectory through a state-dependent medium.

Operational definition. Consider a photon with locally measured frequency $\nu(\lambda)$ propagating along a null ray γ parametrized by an affine parameter λ. We define the observed redshift between emission at $\lambda = \lambda_{\rm e}$ and observation at $\lambda = \lambda_{\rm o}$ by

$$1 + z \;\equiv\; \frac{\nu_{\rm e}}{\nu_{\rm o}} \;=\; \exp\!\left(\int_{\lambda_{\rm e}}^{\lambda_{\rm o}} \mathcal{I}[\chi(x), \nabla\chi(x), u^\mu(x), \ldots]\, \mathrm{d}\lambda\right), \tag{1}$$

where $\chi(x)$ is a medium state variable (e.g. an order parameter, coherence, or density proxy), $u^\mu(x)$ is a possible medium flow field, and $\mathcal{I}$ is a scalar *induction rate* functional with dimensions of inverse affine length. Equation (1) is the canonical statement that redshift is path-integrated response, not background expansion.

Differential form. Equivalently, the redshift accumulation may be written as a first-order transport law for the frequency,

$$\frac{\mathrm{d}}{\mathrm{d}\lambda} \ln \nu(\lambda) \;=\; -\,\mathcal{I}[\chi, \nabla\chi, u^\mu, \ldots]\,, \qquad \Rightarrow \qquad 1 + z = \exp\!\left(-\int_{\lambda_{\rm e}}^{\lambda_{\rm o}} \frac{\mathrm{d}}{\mathrm{d}\lambda} \ln \nu \, \mathrm{d}\lambda\right), \tag{2}$$

so that any nontrivial z arises from a nonzero $\mathcal{I}$ along the ray.

Minimal "state-driven" choice. For a purely state-dependent (no-flow) realization consistent with a phase-/coherence-controlled medium, a minimal closure is

$$\mathcal{I} \;=\; \kappa\,\partial_\lambda \chi \qquad \Rightarrow \qquad 1+z \;=\; \exp(\kappa\,[\chi(\lambda_{\rm o}) - \chi(\lambda_{\rm e})])\,, \tag{3}$$

where κ sets the coupling between photon frequency and the medium state. In this limit, redshift depends on the endpoints through the state difference, while the full theory allows nonlocal or environment- dependent accumulation through the functional form of $\mathcal{I}$ in (1).

Distance is not assumed from redshift. Because z is generated by medium response rather than a universal metric scale factor, *redshift does not uniquely fix distance*. Distance measures (e.g. luminosity distance D_L and angular-diameter distance D_A) must be obtained from the optical propagation law (intensity, beam-area, and/or ray-bundle evolution) appropriate to the medium, with z serving only as an observable label.

Notation and "expansion language." Where convenient, one may introduce an *effective* kinematic mapping (e.g. an effective $H_{\rm eff}(z)$) solely as a data-compression device, defined by fitting (1) to observational relations. Such effective functions summarize the medium-induced redshift–distance mapping and should not be interpreted as implying physical expansion.

2 What Is Meant by "Flow" in the ECSM Model

A central source of confusion when interpreting the ECSM framework concerns the meaning of the term *flow*. In conventional fluids, flow typically implies the transport of material substance from one location to another. In the present model, however, the medium is treated as a *superfluid-like phase field*, and its flow must be understood in a fundamentally different sense.

Specifically, medium flow refers to the collective dynamics of the medium's phase, not to the bulk transport of constituent particles. In superfluid systems, the velocity field is proportional to a phase gradient, while the underlying medium remains globally present and conserved. The motion describes how stresses and excitations propagate through the medium, not how the medium is depleted or accumulated.

Within this framework, gravitational phenomena correspond to spatial variations in the mediums's effective density and flow field, which modify local propagation speeds and inertial response. An inward-directed flow toward a mass concentration therefore does not imply that the medium is being "consumed" by matter, nor that it must accumulate at the center. Instead, such flow patterns represent steady configurations of the phase field, analogous to circulation or compression patterns in known superfluids.

This interpretation resolves a common but misleading intuition: the question of "where the medium goes" arises only if flow is mistakenly equated with material transport. When properly understood as phase-coherent motion within a conserved medium, inward and outward flow patterns can coexist in equilibrium without violating conservation laws.

3 Operational Distance–Redshift Dictionary in a Medium Cosmology

A key departure from the standard FRW interpretation is that the measured redshift z is not assumed *a priori* to be identical to the scale–factor relation $1+z = a_0/a$. Instead, z is treated as an *operational observable* describing how photon frequency evolves along the propagation path through the medium. Consequently, the usual one–line conversions $t(z)$, $D_A(z)$, $D_L(z)$ inherited

from FRW cannot be imported without re-derivation. This section provides the dictionary used throughout Paper 2: (i) the redshift law, (ii) the propagation geometry ("optical metric"), and (iii) the resulting distance measures and consistency relations.

3.1 Redshift as a propagation effect

Consider a photon with wave four-vector k^μ and frequency measured by an observer with four-velocity u^μ,

$$\nu \equiv -\, k_\mu u^\mu. \tag{4}$$

The observed redshift between emission event e and observation event o is defined kinematically by

$$1 + z \equiv \frac{\nu_e}{\nu_o}. \tag{5}$$

In a medium-based cosmology, we do not presume z to encode universal expansion time. Rather, we posit a *redshift evolution law* along the ray parameter λ:

$$\frac{d \ln \nu}{d\lambda} = \mathcal{R}(x^\mu(\lambda), k^\mu(\lambda); \Theta)\,, \tag{6}$$

where Θ denotes model parameters controlling medium response (e.g. density, strain, refractive index, coupling strengths). Equation (6) makes explicit that z is in general a *path integral*:

$$\ln(1+z) = \int_{\lambda_o}^{\lambda_e} \mathcal{R}(x(\lambda), k(\lambda); \Theta)\; d\lambda. \tag{7}$$

When $\mathcal{R}$ reduces to a pure scale–factor term, FRW is recovered as a special case. Otherwise, z cannot be used as a universal clock without an additional mapping derived from the propagation model.

3.2 Propagation geometry and the optical metric

To predict angles, travel times, focusing, and flux transport, the redshift law must be paired with a propagation geometry. We introduce an *effective optical metric* $\tilde{g}_{\mu\nu}$ such that rays satisfy null propagation in $\tilde{g}_{\mu\nu}$:

$$\tilde{g}_{\mu\nu} k^\mu k^\nu = 0, \qquad k^\nu \tilde{\nabla}_\nu k^\mu = 0, \tag{8}$$

where $\tilde{\nabla}$ is the covariant derivative compatible with $\tilde{g}_{\mu\nu}$. Conceptually, $\tilde{g}_{\mu\nu}$ encodes the medium's effective refractive structure and replaces the assumption that photon trajectories are null geodesics of a single background spacetime metric. The matter rest frame is still defined by u^μ (the medium flow), but photon propagation is governed by $\tilde{g}_{\mu\nu}$.

The optical metric provides two essential outputs used below: (i) the mapping between affine parameter λ and observed arrival time (time of flight), and (ii) the evolution of the beam cross-section (focusing), which sets angular and luminosity distances.

3.3 Distance measures: D_A, D_L, and time-of-flight

We use the following operational definitions.

Angular-diameter distance. For a source of physical transverse size $\ell_\perp$ that subtends an observed angle $\delta\theta$, the angular-diameter distance is

$$D_A \equiv \frac{\ell_\perp}{\delta\theta}. \tag{9}$$

Within the optical-metric formalism, D_A is obtained from the Sachs optical equations describing the evolution of the beam expansion θ_b and shear σ_b along the ray:

$$\frac{d\theta_b}{d\lambda} = -\theta_b^2 - |\sigma_b|^2 - \frac{1}{2}\,\tilde{R}_{\mu\nu}k^\mu k^\nu, \tag{10}$$

$$\frac{d\sigma_b}{d\lambda} = -2\theta_b\sigma_b - \tilde{C}_{\mu\alpha\nu\beta}\,m^\mu k^\alpha m^\nu k^\beta, \tag{11}$$

where $\tilde{R}_{\mu\nu}$ and $\tilde{C}_{\mu\alpha\nu\beta}$ are the Ricci and Weyl tensors of $\tilde{g}_{\mu\nu}$, and m^μ is a complex screen basis vector. The area distance is determined by the beam area $\mathcal{A}(\lambda)$ via $D_A \propto \sqrt{\mathcal{A}}$ with standard boundary conditions at the observer.

Luminosity distance. For a source with bolometric luminosity L and observed flux F, the luminosity distance is

$$D_L \equiv \sqrt{\frac{L}{4\pi F}}. \tag{12}$$

In FRW/GR, D_L is related to D_A by Etherington reciprocity, $D_L = (1+z)^2 D_A$, assuming photons follow metric null geodesics and photon phase-space density is conserved. In a medium model, the relation becomes a *diagnostic* rather than an identity. We parameterize potential deviations by

$$D_L = (1+z)^2\, D_A\, \eta(z), \tag{13}$$

where $\eta(z) = 1$ recovers reciprocity and $\eta(z) \neq 1$ captures net dimming/brightening from absorption, scattering, mode conversion, or non-conservation of photon number in the effective medium.

Time-of-flight distance / lookback time. The observed lookback time to redshift z is defined operationally from arrival-time differences between signals and depends on the mapping between λ and observer proper time τ_o along u^μ:

$$\Delta\tau_o = \int_{\lambda_o}^{\lambda_e} \left(\frac{d\tau_o}{d\lambda}\right) d\lambda. \tag{14}$$

Because z is not assumed to be a universal clock, $t(z)$ (or $\tau(z)$) must be derived from the joint system (7)–(8). In particular, any statement about "age" or "distance travelled" must specify which operational distance (angular, luminosity, or time-of-flight) is being referenced.

3.4 Consistency relations and falsifiability

The separation of (i) redshift evolution and (ii) optical propagation yields clear, testable consistency checks:

3.5 Toy BBN consistency scan under the $H(T)$ ansatz

A key early-universe consistency check is whether the model admits a parameter region in which the primordial light-element yields are simultaneously plausible. We implemented a deliberately minimal ("toy") BBN diagnostic designed to test existence of viable parameter space rather than to replace a full nuclear-reaction network.

We evolve the neutron fraction X_n directly as a function of temperature, avoiding an explicit $T(t)$ reconstruction. Assuming a radiation-cooling relation

$$\frac{dT}{dt} \simeq -H(T)\,T, \tag{15}$$

and adopting the phenomenological expansion-rate ansatz

$$H(T) = H_1 \left(\frac{T}{1\ \mathrm{MeV}} \right)^p, \tag{16}$$

the neutron fraction is integrated via

$$\frac{dX_n}{dT} = \frac{(dX_n/dt)}{(dT/dt)}, \tag{17}$$

with a simplified weak-rate model enforcing detailed balance through $\exp(-\Delta m/T)$. The helium-4 mass fraction is then approximated by

$$Y_p \simeq 2X_n(T_{\mathrm{nuc}}), \tag{18}$$

while deuterium is represented by a scaling proxy capturing the dominant degeneracy that higher baryon density suppresses D/H and faster expansion enhances it.

Using observational targets $Y_p = 0.245 \pm 0.003$ and $\mathrm{D/H} = (2.50 \pm 0.05) \times 10^{-5}$, a coarse grid search over $(\eta_{10}, H_1, p, T_{\mathrm{nuc}})$ identifies a viable region. A representative best-fit point within the scanned domain is

$$\eta_{10} = 4.0, \qquad H_1 = 0.200, \qquad p = 2.4, \qquad T_{\mathrm{nuc}} = 0.10\ \mathrm{MeV}, \tag{19}$$

for which the toy model predicts

$$Y_p = 0.2432, \qquad \mathrm{D/H} = 2.51 \times 10^{-5}, \tag{20}$$

with an overall $\chi^2 \simeq 0.40$ under the adopted uncertainties. This demonstrates that the $H(T)$ ansatz admits a parameter region consistent with the gross BBN yield constraints at the level expected for a simplified diagnostic. A full reaction-network implementation is deferred to future work.

1. **Reciprocity test:** infer $D_L(z)$ from standard candles (e.g. SNe Ia) and $D_A(z)$ from standard rulers (e.g. BAO, strong-lens time-delay geometry) and constrain $\eta(z)$ in Eq. (13). Any robust $\eta(z) \neq 1$ is a sharp signal of non-FRW propagation physics.

2. **Multi-messenger time-of-flight:** compare travel-time predictions (from the optical metric) against electromagnetic and gravitational signals when available, probing whether different modes share the same effective geometry.

3. **Overconstrained anchors:** the same parameter set Θ must simultaneously predict the Hubble diagram (D_L), angular ruler measurements (D_A), and the mapping between z and propagation time. This replaces the FRW assumption-set with an explicit, falsifiable map from the medium microphysics to observables.

3.6 Anchor set used in this work

Throughout Paper 2 we treat the following as primary observational anchors: (i) local calibration of signal propagation and clock rates (laboratory and solar-system tests), (ii) standard candles (SNe Ia) constraining $D_L(z)$, (iii) standard rulers (BAO) constraining $D_A(z)$ and combinations of radial/transverse scales, and (iv) the CMB acoustic angular scale θ_*, which constrains the ratio of a physical sound-horizon scale to an angular-diameter distance at last scattering. Importantly, in this framework these anchors constrain *both* the redshift law and the propagation geometry rather than being interpreted through a fixed FRW conversion.

3.7 Interpretational Status of the Cosmic Microwave Background

The Cosmic Microwave Background (CMB), first detected serendipitously by Penzias and Wilson in 1965, constitutes one of the most precisely characterized observational datasets in cosmology. Subsequent measurements by COBE, WMAP, and Planck have established a set of robust empirical properties that any viable cosmological framework must reproduce, independent of interpretational preference.

Foremost among these is the near-perfect blackbody spectrum of the CMB, measured by the COBE/FIRAS instrument to a precision of order 10^{-5}. This observation unambiguously implies that the radiation originated from a system that achieved near-thermal equilibrium prior to decoupling. Importantly, this constraint is thermodynamic in nature and does not, by itself, uniquely specify the mechanism responsible for cooling or energy redistribution.

In addition, the CMB exhibits a high degree of statistical isotropy, with temperature fluctuations at the level of $\Delta T/T \sim 10^{-5}$ across the sky. The dominant dipole anisotropy is well accounted for by the peculiar velocity of the Solar System relative to the CMB rest frame. The absence of detectable parallax, directional asymmetry, or correlation with Galactic structure robustly excludes explanations based on local or Galactic foreground emission. Consequently, the CMB must be regarded as a genuinely global phenomenon.

Perhaps the strongest observational constraints arise from the angular power spectrum and polarization measurements. The presence of multiple acoustic peaks, their relative phases and amplitudes, and the observed TE and EE polarization correlations demonstrate that the radiation emerged from a coupled photon–baryon plasma supporting coherent acoustic oscillations prior to decoupling. These features require a finite sound horizon, phase coherence across modes, and a well-defined effective freeze-out epoch.

While these observations impose stringent constraints on the physical state of the pre-decoupling medium, they do not uniquely determine the underlying mechanism responsible for that state. In particular, the data constrain the thermodynamic and kinematic properties of the plasma at decoupling, but do not by themselves require that those properties arose exclusively through metric expansion of spacetime. Alternative frameworks capable of producing a homogeneous, isotropic medium undergoing a global phase transition with finite sound speed and coherent oscillatory dynamics remain, in principle, observationally viable.

Within the ECSM framework explored in this work, the CMB is interpreted as a genuine thermodynamic relic of a global condensation or transparency transition in a continuous medium. In this picture, the characteristic angular scales traditionally associated with a cosmological sound horizon arise from intrinsic medium properties rather than from spacetime expansion per se. Redshift is correspondingly reinterpreted as an emergent dynamical effect associated with excitation propagation through the medium, rather than as a direct measure of metric stretching. The observational equivalence of these descriptions at the level of the CMB underscores that current data constrain observable correlations and spectra, but do not uniquely fix the underlying ontological mechanism.

Accordingly, the CMB is treated here not as evidence against non-expansion cosmologies, but as a stringent calibration target. Any alternative framework must reproduce its blackbody spectrum, isotropy, acoustic structure, and polarization correlations with quantitative fidelity. The present work adopts this standard, while exploring whether a medium-based dynamical origin can account for the observed phenomenology without invoking fundamental spacetime expansion.

4 Growth of Structure in the ECSM Framework

4.1 From fluid response to an effective growth equation

On sub-horizon scales, the growth of non-relativistic density perturbations can be treated in a Newtonian limit. In standard cosmology, linear growth is governed by the continuity and Euler equations coupled to a Poisson equation for the gravitational potential. In a ECSM framework, the same structure can be retained but with *effective* couplings that encode how the medium transmits (i) inertial response, (ii) potential response, and (iii) dissipationless transport.

"We parameterize the linear medium response governing density growth by two phenomenological ingredients: (i) an effective Hubble-like friction term $H_{\rm eff}(a)$ that controls the dilution/drag of peculiar velocities in comoving coordinates, and (ii) an effective Poisson coupling $\mu(a)$ capturing how strongly density perturbations source the potential within the medium (e.g. $\mu(a) = G_{\rm eff}(a)/G$). In the sub-horizon, pressureless limit, the linear growth factor $D(a)$, defined by $\delta(\mathbf{x}, a) = D(a)\,\delta(\mathbf{x}, a_0)$, obeys the standard-form second-order ODE but with these replacements:

$$\frac{d^2D}{d(\ln a)^2} + \left[2 + \frac{d\ln H_{\rm eff}}{d\ln a}\right]\frac{dD}{d\ln a} - \frac{3}{2}\,\mu(a)\,\Omega_m(a)\,D = 0. \tag{21}$$

Here $\Omega_m(a)$ is defined *relative to the chosen backbone* via

$$\Omega_m(a) \equiv \frac{\Omega_{m0}a^{-3}}{E^2_{\rm eff}(a)}, \qquad E_{\rm eff}(a) \equiv \frac{H_{\rm eff}(a)}{H_0}. \tag{22}$$

Equation (21) is deliberately written to make the separation of roles explicit: the square-bracket term sets the *friction* (how rapidly peculiar velocities decay in comoving coordinates), while the last term sets the *driving* (how strongly matter perturbations seed the potential through the medium).

4.2 Model classes used for numerical diagnostics

For numerical work we consider two broad diagnostic classes:

(A) Conservative backbone (LCDM distances, medium deviation in duality only). We keep $H_{\rm eff}(a)$ equal to a flat-ΛCDM background for the purpose of growth diagnostics and place the medium deviation in the *distance duality* sector (used by SN/BAO fits elsewhere). In this case $\mu(a)$ may still differ from unity and is constrained by growth observables rather than distances.

(B) ECSM growth (medium-driven mapping). We instead take $H_{\rm eff}(a)$ to be the effective mapping implied by the ECSM model used in the distance sector (the same choice used to compute $\chi(z)$ and D_A). In this case Eq. (21) becomes a consistency check: the same backbone must simultaneously match distance measures *and* produce acceptable growth.

In both classes, $\mu(a)$ can be treated either as a constant μ_0 (minimal diagnostic) or as a mild power law $\mu(a) = \mu_0 a^\nu$ (to test whether medium response is scale-time dependent).

4.3 Observable: $f\sigma_8$ and comparison strategy

To connect with data in a backbone-independent way, we compute the growth rate

$$f(a) \equiv \frac{d\ln D}{d\ln a}, \tag{23}$$

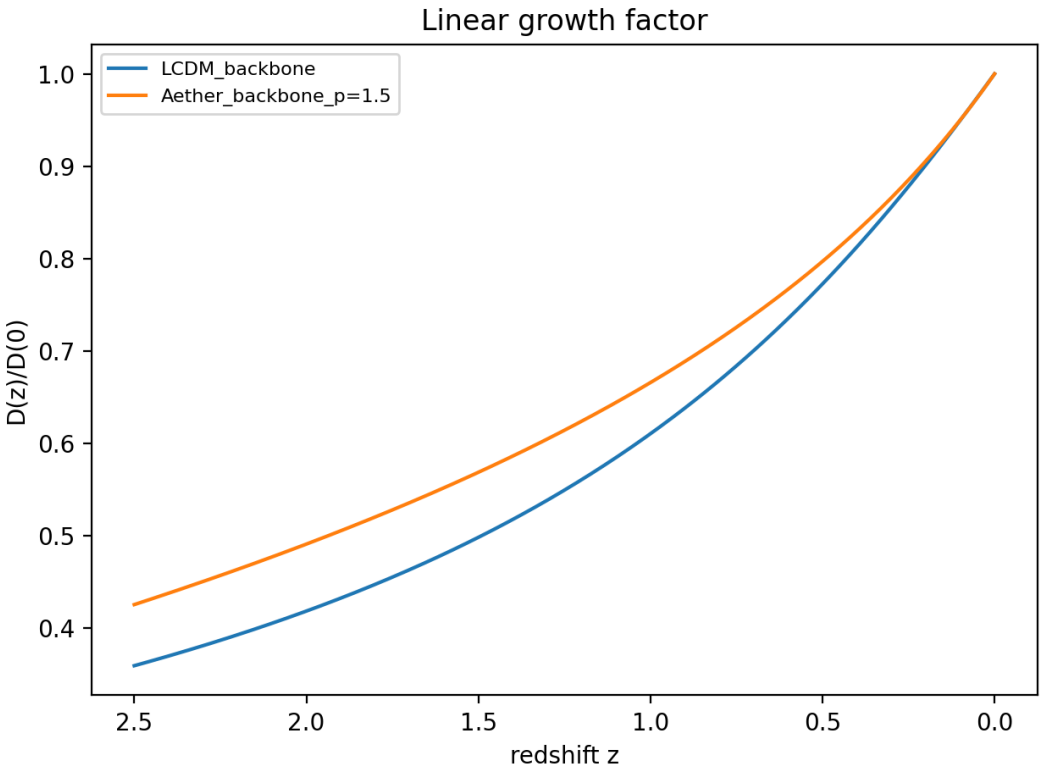

Figure 1: Normalized linear growth factor histories $D(z)/D(0)$ for representative backbones and ECSM-response choices. The diagnostic separates *friction-driven* suppression (via H_{eff}) from *coupling-driven* enhancement (via $\mu(a)$).

and the commonly reported combination

$$f\sigma_8(a) \equiv f(a)\,\sigma_{8,0}\,\frac{D(a)}{D(1)}. \tag{24}$$

In this paper we focus on *shape diagnostics*: whether the ECSM model choices that succeed in distance-sector tests yield a qualitatively reasonable $D(z)$ and $f\sigma_8(z)$ evolution compared to the canonical expectations. A full likelihood analysis against RSD compilations is deferred to later work once the backbone is finalized.

4.4 Results: linear growth histories

Figure 1 shows the normalized growth factor histories $D(z)/D(0)$ for representative backbones and medium-couplings. Figure 2 shows the corresponding $f\sigma_8(z)$ curves. These diagnostics identify which ECSM parameterizations damp growth too strongly (excess friction) or overdrive growth (excess effective coupling), thereby constraining the allowable medium response functions $\mu(a)$.

5 Reinterpreting the Cosmic Microwave Background in a ECSM Framework

The cosmic microwave background (CMB) is commonly interpreted as relic radiation released at photon decoupling in an expanding Friedmann–Lemaître universe. In the present framework, we do not dispute the existence or precision of the observational datasets; rather, we reconsider what

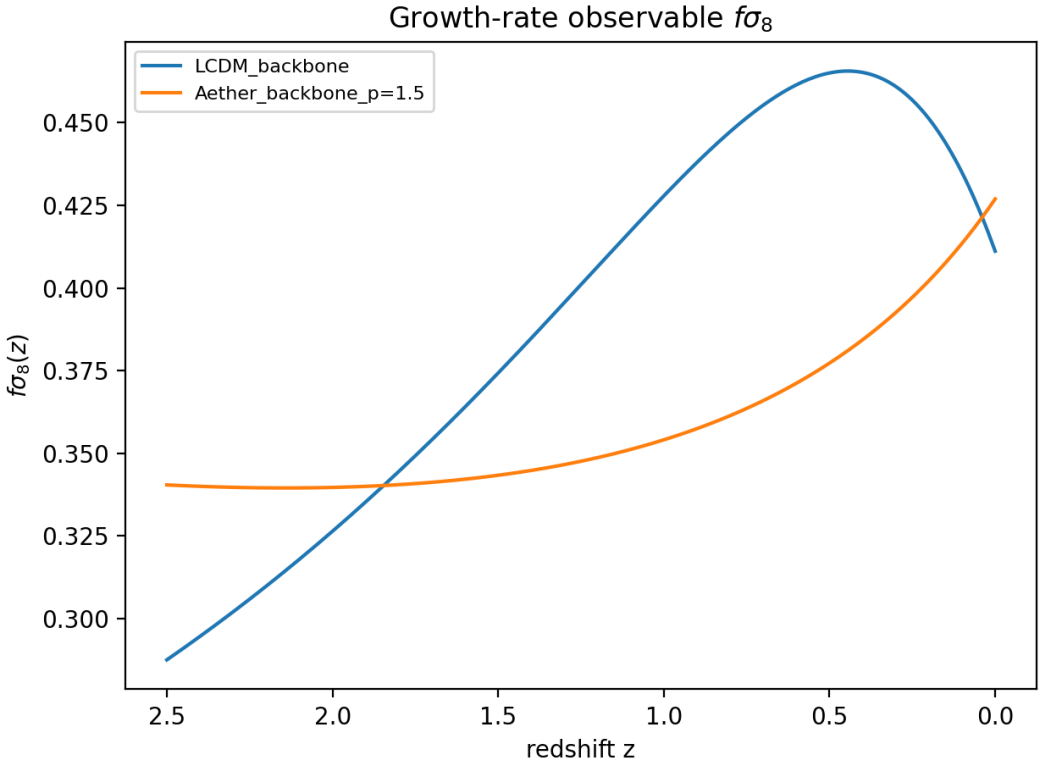

Figure 2: Growth-rate observable $f\sigma_8(z)$ computed from Eq. (24) for the same set of models shown in Fig. 1. This is the quantity most directly comparable to RSD constraints and provides a practical falsification channel for any candidate ECSM-backbone mapping.

the CMB implies about the underlying ontology. Our guiding hypothesis is that a continuous superfluid medium defines a preferred rest frame and supports collective excitation modes that can behave as radiation. Within this picture, the CMB is interpreted as a near-equilibrium excitation bath of the medium, established during an early condensation/relaxation epoch and subsequently observed through weakly perturbed propagation and scattering.

5.1 Blackbody spectrum as global thermalization

The CMB spectrum is extraordinarily close to a Planck distribution with small measured spectral distortions. In the ECSM interpretation this is not taken as direct evidence for metric expansion, but as evidence for (i) an epoch of strong thermalization in a high-opacity phase of the medium and (ii) late-time evolution that preserves near-equilibrium. The observed temperature is treated as an effective equilibrium parameter for the coupled ECSM–radiation sector. Any viable model must therefore suppress frequency-dependent energy injection and predict distortions below current limits.

5.2 Isotropy, dipole, and a preferred rest frame

The large-scale isotropy of the CMB is naturally compatible with a homogeneous background state of the medium. The dominant dipole anisotropy is interpreted kinematically as motion relative to the medium's rest frame, producing Doppler and aberration effects on the excitation bath. In this view the CMB defines a physical frame tied to the medium rather than a purely geometric "comoving" frame.

5.3 Acoustic structure as normal modes of a coupled medium

The angular power spectrum exhibits a series of acoustic peaks usually attributed to standing-wave oscillations in the pre-decoupling photon–baryon plasma. In the ECSM framework, analogous peak structure arises from normal modes of a coupled system comprising baryons and ECSM-supported excitations with an effective sound speed, inertia ratio, and damping scale determined by microphysics (coupling strength, opacity, and transport coefficients). The peak positions constrain an effective horizon scale for coherence in the medium; the relative peak heights constrain the effective inertia and driving/damping mechanisms. Matching the detailed peak structure is thus a quantitative target that can, in principle, be expressed directly in terms of the medium's parameters.

5.4 Polarization, damping, and lensing as transport/propagation effects

CMB polarization (E-modes) and temperature–polarization correlation are interpreted as consequences of anisotropic scattering at the epoch when the medium becomes sufficiently transparent to preserve a last significant interaction surface. The damping tail at high multipoles is attributed to diffusion/viscosity and finite mean-free-path effects in the coupled system, closely analogous to Silk damping but formulated as transport in the Superfluid medium. Gravitational lensing of the CMB is reinterpreted as phase-front/trajectory remapping caused by inhomogeneity in the medium (and baryonic structure), equivalent observationally to an effective refractive or metric response.

5.5 Observational non-uniqueness and discriminating tests

A key point is that several headline CMB features—a near-blackbody spectrum, a global dipole frame, and standing-wave-like angular structure—primarily indicate the existence of a coherent, thermalizing medium with well-defined transport properties. They do not uniquely require metric expansion as the only explanatory mechanism. Discriminating between an expanding-spacetime interpretation and a medium-based interpretation therefore requires targeted predictions: spectral distortion evolution, polarization and lensing consistency, and cross-correlations with late-time structure formation. In later sections we connect these requirements to the model's redshift mechanism and to growth-of-structure diagnostics.

6 What "Quantum" Means in a Medium-Based Framework

Before addressing specific quantum phenomena, it is essential to clarify what is meant by "quantum behaviour" within a medium-based description. In the present framework, quantum effects are not taken as fundamental axioms imposed on nature, but as emergent features of coherent excitations propagating within a structured physical substrate.

In orthodox quantum mechanics, the wavefunction is introduced as a primitive object whose interpretation is probabilistic by postulate. Measurement, collapse, and nonlocal correlations are then added as auxiliary rules, often without an underlying physical mechanism. By contrast, the ECSM framework treats the wavefunction as an effective description of a real, extended excitation of the medium, characterized by amplitude, phase, and coherence.

6.1 Excitations versus particles

In a superfluid or condensate system, localized "particles" are not fundamental objects but long-lived, stable excitation patterns of the medium. Phonons, vortices, and quasiparticles behave as particles in interactions, yet are intrinsically wave-like and spatially extended. The ECSM framework adopts this same ontology: what are ordinarily called particles are interpreted as persistent excitation modes of the underlying medium.

Within this view, the apparent duality between wave-like propagation and particle-like detection is not paradoxical. Wave-like behaviour reflects the distributed nature of the excitation, while particle-like outcomes arise when energy and momentum are irreversibly transferred to localized degrees of freedom during interactions.

6.2 Phase, coherence, and probability

The central quantity governing quantum behaviour in this framework is phase coherence. An excitation propagating through the medium carries a well-defined phase field whose evolution determines interference, superposition, and correlation effects. As long as phase coherence is maintained, the excitation must be described as an extended object, even if its energy density is small or spread over a large region.

Probabilistic outcomes arise not as fundamental indeterminism, but as a consequence of coarse-graining over inaccessible microscopic degrees of freedom. The squared amplitude of the effective wavefunction corresponds to an energy-density or interaction-density measure within the medium, which naturally determines detection statistics when interactions occur.

6.3 Measurement as medium reconfiguration

Measurement is not treated as a special or non-physical process. Instead, it is understood as a dynamical coupling between a coherent excitation and a macroscopic system with many internal degrees of freedom. This coupling generically leads to rapid decoherence, in which phase information is dispersed into the medium and becomes effectively unrecoverable.

In this sense, "collapse" is not a literal instantaneous change of state across space, but the local and irreversible reconfiguration of the medium due to interaction. After decoherence, the excitation can no longer be described as a single coherent mode, and a classical outcome emerges.

6.4 Emergent quantum rules

Within this framework, the familiar rules of quantum mechanics arise as effective, low-energy descriptions of medium dynamics:

- Wave equations reflect the propagation of collective modes.
- Superposition reflects linearity in the weak-excitation regime.
- Interference reflects phase coherence.
- Measurement reflects decoherence through coupling to macroscopic structures.

No additional postulates beyond the existence of a coherent medium and its excitation spectrum are required. Quantum behaviour is therefore not imposed, but emerges naturally from the dynamics of the Superfluid medium in the same way that phonons, vortices, and superfluid flow emerge in known condensed-matter systems.

This interpretation provides the conceptual foundation for the analysis of specific quantum phenomena developed in the following sections.

7 Core Quantum Phenomena as Medium Dynamics

Having clarified the meaning of quantum behaviour in a medium-based framework, we now examine how the principal quantum phenomena arise naturally from the dynamics of a coherent Superfluid medium. The goal of this section is not to modify quantum predictions, but to provide a physically grounded interpretation that eliminates conceptual paradoxes without altering empirical success.

7.1 Wave–particle duality

In the ECSM framework, wave–particle duality is not a duality of ontology but of description. All propagating entities are fundamentally wave-like excitations of the medium. Apparent particle behaviour emerges only during interactions that localize energy and momentum transfer.

An excitation propagating through the medium is spatially extended and governed by a wave equation. When such an excitation encounters a localized interaction region (e.g. a detector, atom, or scattering center), energy is transferred discretely, producing a localized event. The discreteness arises from the quantized interaction channels of the medium, not from point-like particles traveling through empty space.

Thus, wave-like propagation and particle-like detection are complementary manifestations of the same underlying process: coherent excitation followed by localized dissipation.

7.2 Superposition

Superposition arises from the linear response of the medium in the weak-excitation regime. When multiple propagation paths or modes are available, the excitation naturally occupies all of them simultaneously as a distributed phase-coherent state.

In this framework, superposition does not imply that a system exists in multiple classical states at once. Rather, it reflects the fact that the excitation has not yet been forced into a localized configuration by interaction with a macroscopic system. As long as coherence is preserved, the excitation must be treated as a single extended object whose phase evolution encompasses all allowed paths.

The breakdown of superposition occurs dynamically through decoherence, not through an ad-hoc collapse rule.

7.3 Interference

Interference is a direct consequence of phase coherence within the medium. When an excitation propagates along multiple paths, the phase accumulated along each path determines the local energy density upon recombination. Regions of constructive and destructive interference correspond to reinforcement or cancellation of the underlying medium oscillations.

Crucially, interference does not require self-interaction or multiple particles. Even single-excitation experiments exhibit interference because the excitation itself is spatially extended and phase-coherent. This behaviour is identical to that observed in phonon propagation, surface waves, and other well-understood classical wave systems, with quantization entering only at the level of interaction.

7.4 Decoherence and the emergence of classicality

Decoherence occurs when an excitation becomes entangled with many uncontrolled degrees of freedom in the surrounding medium or environment. This process disperses phase information into microscopic modes, rendering interference between macroscopically distinct configurations unobservable.

In the ECSM framework, decoherence is a physical process governed by coupling strength, interaction time, and medium properties. No observer-dependent postulate is required. Classical behaviour emerges whenever coherence length and coherence time become much smaller than the relevant observational scales.

Macroscopic objects appear classical because they are continuously and strongly coupled to the medium, preventing the formation of long-lived coherent excitation states.

7.5 Measurement without collapse

Measurement is interpreted as an extreme case of decoherence accompanied by irreversible energy transfer. The outcome of a measurement corresponds to the specific localized configuration of the medium that results from this interaction.

There is no instantaneous global collapse of a wavefunction. Instead, the effective description transitions from a coherent excitation to an incoherent statistical mixture due to physical processes occurring at the interaction site. Apparent nonlocal updates in state descriptions reflect changes in information, not superluminal physical effects.

This resolves the measurement problem by embedding it entirely within ordinary dynamics of a physical medium.

8 Relativistic Consistency and the No-Signaling Principle

A common objection to any theory positing an underlying medium is that it appears to conflict with special relativity. In particular, concerns arise regarding the existence of a preferred frame, the invariance of physical laws between observers, and the causal structure of spacetime. In this section we show that the present framework remains fully consistent with relativistic phenomenology at observable scales, while reinterpreting relativity as an emergent symmetry rather than a fundamental principle.

8.1 Emergent Lorentz invariance

In the ECSM framework, Lorentz invariance arises as an effective symmetry of the low-energy excitations of the medium. Collective modes propagate with an approximately linear dispersion relation,

$$E^2 \simeq c_{\text{eff}}^2 p^2 + \mathcal{O}\left(\frac{p^4}{\Lambda^2}\right), \tag{25}$$

where Λ is a high-energy cutoff scale associated with the microphysics of the medium. At energies well below Λ, the higher-order terms are negligible and the dynamics are indistinguishable from those of a relativistic field theory.

This mechanism is well known in condensed-matter analogues, where quasiparticles in a medium exhibit emergent Lorentz symmetry despite the presence of a preferred rest frame at the microscopic level. The same logic applies here: while the superfluid medium defines a preferred structure, its effects are dynamically hidden in the low-energy regime.

8.2 Preferred frame and observational invisibility

Although the medium defines a natural rest frame, no experiment confined to low energies can operationally detect it. This is because all rods, clocks, and signal carriers are themselves excitations of the same medium and are therefore subject to the same effective geometry.

Any attempt to measure motion relative to the Superfluid medium reduces to comparing propagation speeds of excitations, which are governed by the same local value of c_{eff} in all directions. As a result, standard Michelson–Morley–type experiments yield null results, consistent with observation.

Preferred-frame effects, if present at all, are suppressed by powers of E/Λ and are expected to appear only in extreme regimes such as high-energy astrophysics or precision laboratory tests probing dispersion and anisotropy.

8.3 Causality and signal propagation

Causal structure in this framework is determined by the effective metric $g_{\mu\nu}^{\text{eff}}$ derived from the medium state. Signals propagate along null or timelike curves of this emergent geometry, ensuring a well-defined causal ordering of events.

While the underlying medium may support instantaneous or superluminal adjustments at the microphysical level, these do not translate into operationally accessible signaling channels. Observable signals are carried only by collective excitations, whose maximum propagation speed is bounded by c_{eff}.

Thus, macroscopic causality is preserved even if the substrate itself exhibits dynamics outside the effective relativistic description.

8.4 No-signaling and quantum correlations

As discussed in Section 6, entangled correlations arise from global coherence of the medium rather than from signal exchange. This structure automatically satisfies the no-signaling theorem.

Local measurement outcomes depend on uncontrollable microscopic details of the medium–detector interaction and therefore appear statistically random. Although joint statistics reveal strong correlations, no local operation can influence marginal distributions at a distant location.

This explains why quantum mechanics permits violations of Bell inequalities without allowing faster-than-light communication: the correlations reflect shared structure, not causal influence.

8.5 Consistency with relativistic quantum experiments

All experimentally verified relativistic quantum phenomena—including time dilation of unstable particles, relativistic covariance of scattering amplitudes, and Lorentz- invariant quantum field predictions—are reproduced in the emergent regime of the medium.

In this view, relativity is not a statement about the absence of underlying structure, but about the universality of the effective laws governing observable excitations. The success of relativistic quantum theory thus constrains the symmetry properties of the superfluid medium in the low-energy limit, rather than ruling out its existence.

8.6 Summary

The presence of a physical medium does not undermine relativity, causality, or quantum no-signaling. Instead, these principles emerge as robust, low-energy consequences of a highly symmetric ground state.

Relativity is reinterpreted as an effective symmetry of excitations rather than a fundamental property of spacetime itself, while quantum nonlocality is understood as global coherence within a single substrate. This resolves longstanding conceptual tensions without altering any experimentally confirmed predictions.

9 Quantum Fields as Collective Modes of the ECSM

In standard quantum field theory, fields are treated as fundamental entities whose excitations correspond to particles. While enormously successful operationally, this approach leaves open the question of what fields physically are. In the present framework, quantum fields are reinterpreted as collective excitation modes of the underlying superfluid medium, with particles emerging as stable or metastable patterns of medium disturbance.

9.1 Field quantization as mode decomposition

The superfluid medium is characterized at the microscopic level by a small number of fundamental degrees of freedom, such as density, phase, and possibly additional internal variables. Linearizing the dynamics about a homogeneous background yields a spectrum of normal modes, each characterized by a dispersion relation $\omega(\mathbf{k})$.

Quantization arises by decomposing these modes into harmonic oscillators, exactly as in conventional field theory. Creation and annihilation operators correspond to adding or removing quanta of collective excitation, not to manipulating abstract fields existing independently of a substrate.

In this sense, quantization is not imposed but emerges naturally from the mode structure of the medium.

9.2 Particle species and internal quantum numbers

Different particle species correspond to distinct branches of the excitation spectrum. For example, scalar, vector, and fermionic excitations may arise from different symmetry sectors of the medium or from topologically protected modes.

Internal quantum numbers such as charge, spin, and flavor are associated with symmetry properties of the superfluid medium's ground state and its excitations. Gauge symmetries appear as redundancies or invariances in the effective description of these modes, rather than as fundamental forces acting in empty space.

This interpretation aligns with the success of gauge theories while grounding them in physical structure.

9.3 Mass generation and dispersion

In this framework, mass corresponds to a deviation from linear dispersion at low momenta. For a generic excitation mode,

$$\omega^2 = c_{\text{eff}}^2 k^2 + m_{\text{eff}}^2 c_{\text{eff}}^4 + \mathcal{O}\left(\frac{k^4}{\Lambda^2}\right), \tag{26}$$

where m_{eff} is an effective mass parameter determined by medium properties such as compressibility, stiffness, or coupling to background fields.

Thus, mass is not an intrinsic attribute of a particle but an emergent response of the medium to perturbations. This provides a physical interpretation of inertial mass and links naturally to the discussion of inertia and resistance to acceleration.

9.4 Interactions as nonlinear medium dynamics

Particle interactions arise from nonlinearities in the ECSM equations of motion. When multiple excitations coexist, they modify the local medium state, altering propagation and inducing effective forces between modes.

At low energies, these interactions reproduce the perturbative structure of quantum field theory, including scattering amplitudes and effective potentials. At higher energies, deviations from standard behavior are expected as the underlying medium structure becomes relevant.

This perspective explains why renormalization works so well: the effective theory is insensitive to microphysical details until energies approach the cutoff scale Λ.

9.5 Vacuum fluctuations and zero-point energy

In conventional quantum field theory, the vacuum is associated with infinite zero-point energy requiring regularization. In a medium-based description, the vacuum corresponds to a specific ground state of the superfluid medium with finite energy density.

Fluctuations about this ground state manifest as quantum noise, but their spectrum is naturally regulated by the microphysical scale Λ. This provides a physical rationale for vacuum regularization and suggests a route toward resolving the cosmological constant problem, though a full treatment lies beyond the scope of this paper.

9.6 Relation to curved spacetime and gravity

Because excitations propagate on the effective metric $g_{\mu\nu}^{\text{eff}}$, quantum fields automatically experience gravity as geometry. Coupling between quantum fields and gravity thus requires no additional postulates: it is built into the medium description from the outset.

This unifies quantum field theory and gravitation at the effective level, while postponing the need for a full quantum theory of the medium itself.

9.7 Summary

Quantum fields and particles emerge as collective excitations of a single physical substrate. Quantization reflects mode structure, mass arises from dispersion, interactions from nonlinear dynamics, and gravity from the effective geometry governing propagation.

This reinterpretation preserves all tested predictions of quantum field theory while providing a concrete physical picture that connects quantum phenomena, inertia, and gravity within a unified framework.

10 Novel Predictions and Falsifiability

Any viable physical theory must do more than reinterpret existing results: it must make clear, falsifiable predictions that distinguish it from competing frameworks. The ECSM-based interpretation developed in this paper reproduces all experimentally tested predictions of quantum mechanics and relativistic quantum field theory in their appropriate regimes. However, it also leads to specific departures and signatures that can, in principle, be tested.

10.1 Energy-dependent deviations from Lorentz invariance

Because Lorentz symmetry is emergent rather than fundamental, it is expected to break down gradually as probe energies approach the microphysical scale Λ. This leads to modified dispersion relations of the form

$$E^2 = c_{\text{eff}}^2 p^2 + m_{\text{eff}}^2 c_{\text{eff}}^4 + \alpha \frac{p^4}{\Lambda^2} + \cdots , \tag{27}$$

where α is a dimensionless coefficient determined by the medium dynamics.

Such corrections can be constrained through:

- High-energy astrophysical observations (gamma-ray bursts, cosmic rays)
- Precision interferometry
- Laboratory tests of dispersion and anisotropy

Existing bounds place strong lower limits on Λ, but do not eliminate the possibility of emergent Lorentz symmetry.

10.2 Small violations of equivalence at high energies

As discussed earlier, universal coupling arises naturally in the low-energy regime. However, suppressed non-universal operators may appear at order $(E/\Lambda)^n$. This leads to possible deviations from exact universality of free fall in extreme conditions.

Observable consequences could include:

- Composition-dependent phase shifts in high-precision atom interferometers
- Energy-dependent gravitational coupling in strong-field astrophysical systems
- Deviations from standard gravitational wave propagation at high frequencies

These effects are negligible in current experiments but provide clear falsifiability targets.

10.3 Modified vacuum fluctuations

Because the vacuum corresponds to a physical ground state of the medium rather than an abstract zero-point field, its fluctuation spectrum is naturally regulated. This suggests possible deviations from standard quantum vacuum behavior, including:

- Altered Casimir-force scaling at very short distances
- Modified noise spectra in ultra-sensitive interferometers
- Suppression of ultraviolet vacuum divergences

Precision measurements of quantum noise and vacuum forces offer a potential window into the microphysics of the medium.

10.4 Correlated decoherence effects

If entangled systems are supported by a shared medium excitation, decoherence may exhibit weak correlations across spatially separated subsystems. While such effects must be extremely small to remain consistent with existing experiments, they could manifest as:

- Subtle departures from purely local decoherence models
- Environment-dependent entanglement lifetimes
- Long-range phase correlations under controlled conditions

Detecting such effects would provide strong evidence for an underlying physical substrate.

10.5 Gravitational backreaction on quantum coherence

Because quantum excitations propagate on an effective geometry sourced by the medium, strong gravitational environments may influence quantum coherence in novel ways. This includes:

- Gravitationally induced phase shifts beyond standard relativistic predictions
- Environment-dependent decoherence near massive bodies
- Potential signatures in interferometry near compact objects

These effects are negligible in weak fields but become relevant in regimes inaccessible to purely geometric descriptions.

10.6 Distinction from standard interpretations

Crucially, these predictions do not arise from reinterpretation alone. They stem directly from the physical assumption of an underlying medium with finite stiffness, nonlinear response, and a high-energy cutoff. If none of the above deviations are ever observed, and Lorentz symmetry, equivalence, and vacuum behavior remain exact at arbitrarily high energies and precision, the ECSM framework would be ruled out.

Conversely, detection of any one of these effects would provide strong evidence that quantum phenomena emerge from a deeper physical substrate.

10.7 Summary

The ECSM-based framework is fully compatible with all existing quantum and relativistic experiments while making concrete, falsifiable predictions beyond the standard model. These predictions define a clear experimental program through which the theory can be tested, constrained, or rejected.

Falsifiability is not an afterthought in this approach; it is a direct consequence of treating quantum phenomena as emergent dynamics of a physical medium.

11 Quantum Entanglement in a Medium-Based Framework

Entanglement is widely regarded as the most challenging phenomenon for any realist or medium-based interpretation of quantum mechanics. Violations of Bell inequalities are often interpreted as evidence that nature is fundamentally nonlocal or that physical properties do not exist prior to measurement. In this section, we show that neither conclusion is required in an ECSM-based framework.

11.1 Origin of entanglement

In the present model, entanglement arises when multiple excitations are created through a single coherent interaction within the medium. Such a process imprints correlated phase and amplitude information across spatially separated regions of the superfluid medium.

Importantly, the correlations are established at the moment of creation, not during subsequent measurement. Once formed, the joint excitation must be described as a single extended state of the medium, even if its support spans macroscopic distances.

Thus, entanglement reflects the inseparability of the underlying medium excitation, not a mysterious influence propagating between distant objects.

11.2 Why Bell inequalities are violated

Bell inequalities rely on assumptions of statistical independence and local hidden variables assigned to subsystems. In a medium-based framework, these assumptions fail because the subsystems are not independent: they are manifestations of a single coherent state.

Measurement outcomes depend on:

- The shared phase structure of the medium excitation
- Local measurement settings
- The interaction dynamics between detector and medium

Because the phase correlations are non-factorizable, joint probability distributions violate Bell inequalities while remaining entirely causal. No signal or influence is exchanged at the time of measurement; only correlations already encoded in the medium are revealed.

11.3 No superluminal signaling

Despite strong correlations, entanglement does not allow faster-than-light communication. In the ECSM framework, this follows naturally from two facts:

1. Measurement outcomes at each location are locally random due to uncontrollable microscopic degrees of freedom in the medium.
2. The correlated structure becomes apparent only when classical information from both measurement sites is compared.

Thus, while the medium state is globally coherent, locally accessible information remains causally constrained. This mirrors the operational predictions of standard quantum mechanics while providing a clear physical picture.

11.4 Relativity and preferred structure

The presence of an underlying medium does not reintroduce observable preferred-frame effects. Entangled correlations are invariant under changes of inertial frame because they are encoded in the phase relations of the excitation, not in signal propagation.

At the effective level, relativistic symmetry emerges from the low-energy isotropy of the medium. Violations of Lorentz symmetry, if present at all, are suppressed by the same high-energy scale Λ that controls dispersion and equivalence-principle deviations.

Thus, entanglement remains compatible with relativistic causality without invoking fundamental spacetime nonlocality.

11.5 Comparison with alternative interpretations

Unlike Copenhagen interpretations, this framework requires no observer-dependent collapse. Unlike many-worlds interpretations, it does not require branching universes. Unlike superdeterministic models, it does not require conspiratorial correlations in initial conditions.

Entanglement is instead understood as a real, physical coherence within a single substrate. The mystery shifts from abstract probability space to concrete medium dynamics, where it can be studied, modeled, and potentially constrained experimentally.

11.6 Summary

Entanglement, often viewed as the strongest argument against physical realism, becomes a natural and unavoidable consequence of coherent medium dynamics. Bell violations arise because the underlying state is genuinely non-separable, not because nature permits nonlocal causation.

This interpretation preserves all quantitative predictions of quantum mechanics while eliminating the conceptual tension between realism, causality, and observed correlations.

12 Steady-State Configurations and Energy Accounting

A recurrent concern for any flow-based gravitational model is whether the proposed configurations are dynamically stable and energetically consistent. If gravitational effects are associated with inward-directed medium flow toward concentrations of mass, one may ask why the medium does not continuously accumulate, dissipate, or "run down" over time. Here we outline why the superfluid medium admits steady-state solutions in which energy is conserved and macroscopic gravitational configurations persist indefinitely.

12.1 Continuity and steady-state solutions

At macroscopic scales, the superfluid medium is assumed to obey a continuity equation expressing local conservation of the medium,

$$\partial_t n + \nabla \cdot (n\mathbf{v}) = 0, \tag{28}$$

where $n(\mathbf{x}, t)$ is an effective medium density and $\mathbf{v}(\mathbf{x}, t)$ is the associated flow field. In static or quasi-static regimes the time derivative is negligible, $\partial_t n \approx 0$, leading to

$$\nabla \cdot (n\mathbf{v}) = 0. \tag{29}$$

This permits nontrivial stationary configurations in which inward and outward components of the phase flow balance globally.

12.2 Compression, stiffness, and energy storage

In the ECSM framework, energy associated with gravity is stored as elastic and compressional energy of the medium. A schematic effective energy density can be written as

$$\mathcal{E} = \mathcal{E}_0(n) + \frac{1}{2}\kappa\,|\nabla n|^2 + \frac{1}{2}n|\mathbf{v}|^2, \tag{30}$$

where $\mathcal{E}_0(n)$ captures internal energy, κ is a stiffness parameter, and the final term represents coherent-flow energy. Gravitational configurations correspond to (meta)stable minima of an appropriate coarse-grained functional subject to boundary conditions imposed by baryonic matter.

12.3 Recirculation and global balance

While flow may be inward-directed over wide radial ranges, this does not imply a singular endpoint. Superfluid systems generically admit vortical and recirculating components that redistribute phase gradients without requiring a material sink. At macroscopic scales, the gravitational field should be understood as a self-maintaining configuration of the medium rather than a drain on it. This resolves the apparent "pile-up" problem without introducing external sinks or violating conservation laws.

13 Canonical Medium Response and Diagnostic Tests

13.1 Minimal Medium-Response Closure

13.2 Radial Acceleration Relation and Deep-Regime Slopes

13.3 Baryonic Tully–Fisher Scaling

13.4 External Field Effect as Medium Saturation

13.5 Consistency and Limitations

13.6 Response-Function Reconstruction and Curve Collapse

Rather than assuming a specific interpolating function a priori, we perform a reconstruction of the effective medium response directly from the numerical solutions. At each radius we define an empirical response factor

$$\nu_{\rm eff}(r) \equiv \frac{g(r)}{g_N(r)}, \tag{31}$$

and an associated dimensionless control variable

$$x(r) \equiv \frac{g_N(r) + g_{\rm ext}}{a_0}, \tag{32}$$

where g_N is the Newtonian acceleration sourced by the enclosed baryonic mass and $g_{\rm ext}$ represents an externally imposed background field.

If the dynamics are governed by a universal medium response, independent of radius or galaxy mass, then $\nu_{\rm eff}$ evaluated at different radii should collapse onto a single curve when plotted against x. This provides a stringent internal consistency check that does not rely on fitting rotation curves directly.

In Fig. X we demonstrate this collapse for the numerical solutions presented above. Points spanning multiple decades in radius and acceleration fall on a single monotonic response curve, validating the existence of a well-defined effective response function in the medium-dominated regime.

13.7 Application to Observed Rotation Curves

To assess whether the canonical medium response extends beyond idealized toy models, we apply the same diagnostic framework to observed galaxy rotation curves. As a first test, we consider individual galaxies from the SPARC database, which provides resolved rotation curves alongside baryonic mass models.

From the observed circular velocity $v_{\rm obs}(r)$ we construct the total centripetal acceleration

$$g_{\rm obs}(r) = \frac{v_{\rm obs}^2(r)}{r}, \tag{33}$$

while the Newtonian baryonic contribution $g_N(r)$ is obtained directly from the tabulated mass models. No dark matter component is included.

Using the same reconstruction procedure as in Section 13.6, we compute the empirical response $\nu_{\rm eff}(r) = g_{\rm obs}(r)/g_N(r)$ and compare it against the dimensionless control variable $x = (g_N + g_{\rm ext})/a_0$.

This approach allows the medium response to be tested independently of detailed profile fitting, focusing instead on whether observed galaxies occupy the same response curve as the numerical solutions.

14 Emergent Inertia from Superfluid-Medium Interaction

Having established that gravitational configurations correspond to steady deformations of the superfluid medium, we address the origin of inertia. In this framework, inertia emerges from the energetic cost of reconfiguring the medium under acceleration.

14.1 Resistance to acceleration

A localized mass embedded in a steady superfluid medium configuration is surrounded by a stationary pattern of density gradients and flow. Accelerating the mass requires reorganizing this pattern. Because the medium is assumed to be coherent and stiff at macroscopic scales, such reconfiguration incurs an energetic cost and produces restoring stresses opposing the change. Schematically, the inertial response can be viewed as proportional to the time rate of change of momentum stored in the local medium configuration,

$$\mathbf{F}_{\rm inertial} \sim \frac{d}{dt} \int d^3x \, n(\mathbf{x}) \, \mathbf{v}(\mathbf{x}). \tag{34}$$

14.2 Persistence of uniform motion

Once a mass and its associated superfluid medium's configuration are co-moving, no further reconfiguration is required. Uniform motion corresponds to a translated steady state. In this sense, a body in motion remains in motion because the combined matter–medium state has no preferred decay channel in the non-dissipative regime.

14.3 Equivalence of inertial and gravitational mass

Because both gravitational attraction and inertial resistance arise from the same matter–medium interaction, their proportionality is no longer mysterious. Gravitational mass quantifies how matter biases the surrounding medium, while inertial mass quantifies resistance of that biased configuration to change. This provides a natural route to the observed equivalence at low energies.

15 Why Local Physics Appears Lorentz-Invariant

A common objection to medium-based models is apparent conflict with local Lorentz invariance. In the present framework, Lorentz invariance is emergent: low-energy excitations propagate with an approximately linear dispersion,

$$\omega^2 \simeq c_{\text{eff}}^2 k^2, \tag{35}$$

so the governing equations take the same form as relativistic wave equations with invariant speed c_{eff}. Measuring devices and signals are built from the same substrate, so co-moving frames cannot detect absolute motion through the superfluid medium in the low-energy regime. Deviations are expected only near a high-energy cutoff scale Λ where microstructure becomes relevant, providing a path to falsifiability.

Interpretive note: fields as excitation modes of the ECSM The following remarks clarify how familiar field degrees of freedom may be interpreted within the present medium-based framework, without introducing additional fundamental entities.

In the framework considered here, the ECSM is treated as a single continuous medium described by an order parameter $\Psi(\mathbf{x}, t) = \sqrt{n(\mathbf{x}, t)}\, e^{i\theta(\mathbf{x},t)}$, with n denoting an effective density and θ a phase variable. The corresponding superfluid velocity is

$$\mathbf{v} = \frac{\hbar}{m_a} \nabla\theta, \tag{36}$$

where m_a is an effective mass scale associated with the medium. This formulation admits a natural decomposition into distinct excitation modes, which can be interpreted as effective "fields" at macroscopic scales.

Longitudinal compressional response modes. Small perturbations about a homogeneous background, $n = n_0 + \delta n$ and $\theta = \theta_0 + \delta\theta$, give rise to longitudinal density and phase excitations. In the long-wavelength limit, these obey a wave equation of the form

$$\partial_t^2(\delta n) = c_s^2 \nabla^2(\delta n), \tag{37}$$

where c_s is an effective sound speed set by the background medium. These compressional modes provide a natural realization of scalar-field behavior, with the effective "field" corresponding to fluctuations of the medium itself rather than an independent fundamental entity.

Gravitational response as background configuration. Large-scale, slowly varying configurations of the superfluid medium—including spatial variations in density, sound speed, or steady flow—act as a background on which smaller excitations propagate. In this regime, the effective dynamics of perturbations may be expressed in terms of an emergent metric determined by the medium properties. Gravitational acceleration can then be understood as arising from gradients in the background configuration, schematically

$$\mathbf{g} \;\propto\; -\nabla\Phi(n, c_s), \tag{38}$$

where Φ is an effective potential constructed from local ECSM properties. In this view, gravity corresponds to a structural response of the medium rather than a distinct fundamental interaction.

Vortical and vector-like modes. While the superfluid flow is locally irrotational, $\nabla \times \mathbf{v} = 0$, topological defects such as quantized vortices introduce localized circulation. These vortical excitations constitute a separate sector of the dynamics and provide an analogue of vector or gauge-like behavior, with effective "magnetic" structure associated with nonzero vorticity. Importantly, such modes arise as excitations of the same underlying medium, not as independent degrees of freedom.

Emergent relativistic behavior. At sufficiently low energies and long wavelengths, many excitations of the medium exhibit approximately linear dispersion relations, $\omega^2 \simeq c_{\text{eff}}^2 k^2$, yielding an emergent Lorentz-like symmetry with an effective limiting speed c_{eff}. Deviations from exact Lorentz invariance appear only at higher energies where the microscopic structure of the medium becomes relevant. This naturally explains why relativistic behavior is robust for ordinary motion while remaining emergent rather than fundamental.

Relation to matter degrees of freedom. In the present work, baryonic matter is treated phenomenologically as a source that couples to and perturbs the superfluid medium's configuration. A natural extension of the framework is to model matter itself as stable, localized excitations (such as solitons or topological defects) of the same order parameter. In that case, both "fields" and "particles" would correspond to different excitation sectors of a single substrate. This possibility is noted here as an outlook, but is not required for the illustrative results presented in this paper.

16 Illustrative Simulations and Observational Anchors

The purpose of this section is to demonstrate that the mechanisms proposed in Paper I admit explicit realizations that reproduce key qualitative features of observed astrophysical systems. The simulations are intentionally simplified and should be interpreted as existence proofs rather than precision fits.

16.1 Toy rotation curves from baryon-coupled response

Figure **??** shows an illustrative toy rotation curve in which a baryonic-only profile declines with radius while an additional medium-response term yields an extended approximately flat region. The precise functional form is not a claim about microphysics; rather, it demonstrates that steady superfluid medium response can produce the correct qualitative behavior without non-baryonic halos.

16.2 BTFR diagnostic as a coupling constraint

A key empirical constraint is the baryonic Tully–Fisher relation (BTFR), $v_{\text{flat}}^4 \propto M_b$. Figure 5 shows a simple diagnostic comparing a "constant-response" toy model to a baryon-coupled response model. The latter yields a slope close to unity in $\log(v_{\text{flat}}^4)$ versus $\log(M_b)$, whereas constant response fails. This indicates that BTFR tightness can be understood as a structural constraint on the coupling between baryons and the medium response.

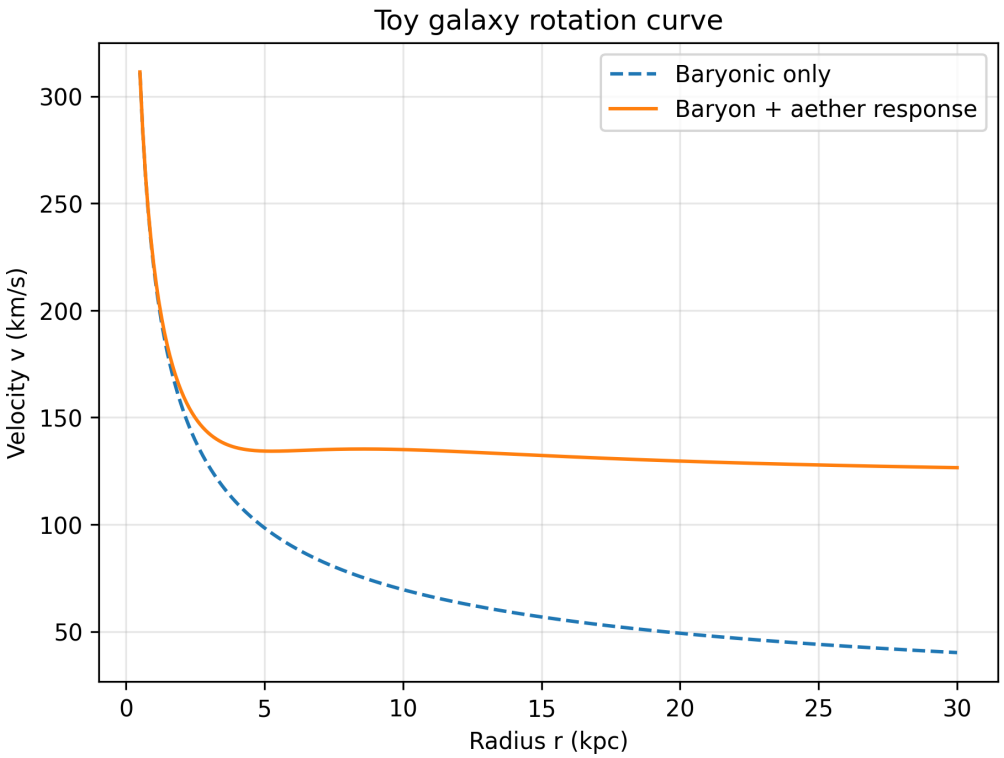

Figure 3: Toy rotation curve (illustrative). The baryonic-only contribution declines with radius, while a baryon-coupled superfluid medium-response term produces an extended approximately flat region.

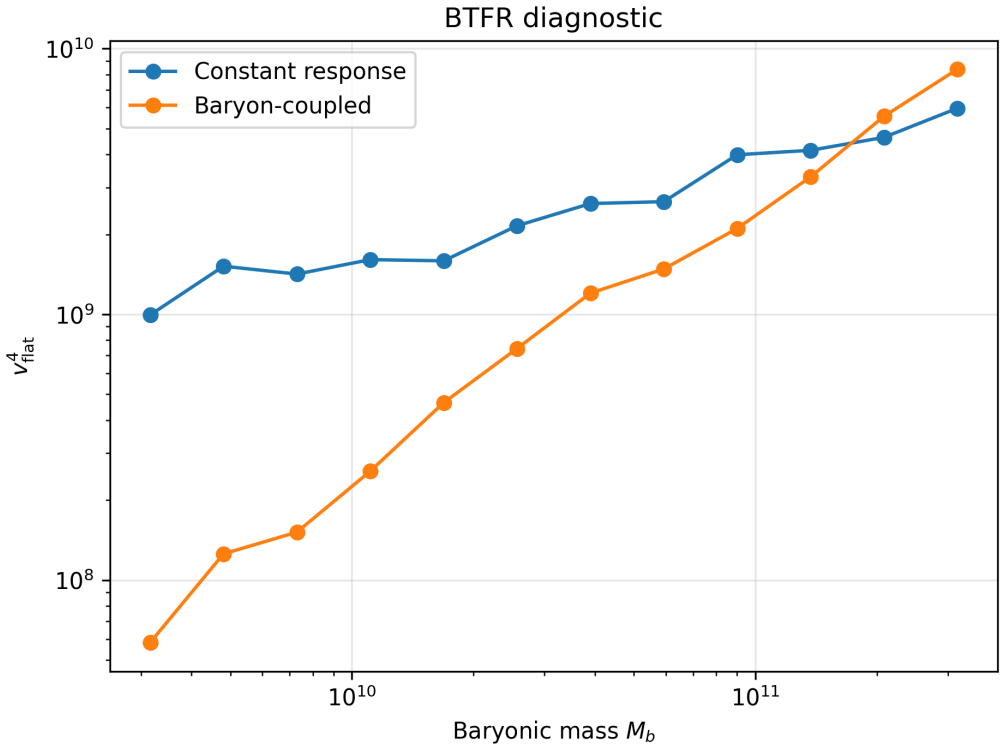

Figure 4: BTFR diagnostic (illustrative). The baryon-coupled response yields a near-unity slope in $\log(v^4_{\rm flat})$ vs $\log(M_b)$, while a constant-response model does not.

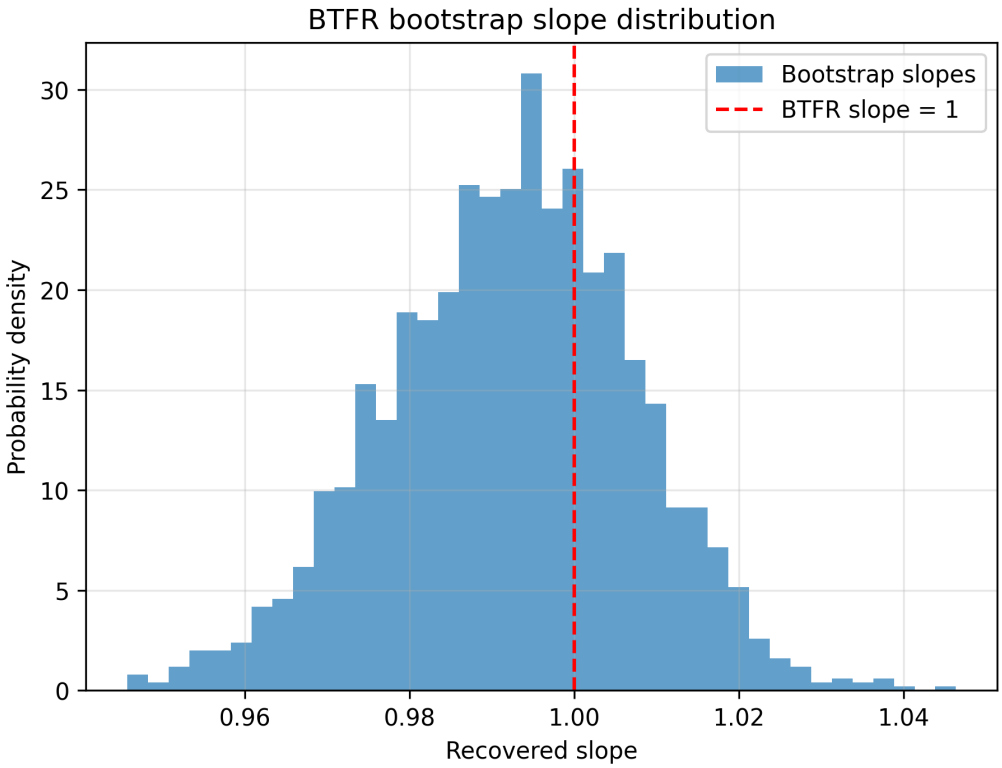

Figure 5: BTFR bootstrap slope distribution (illustrative). Distribution of recovered slopes from bootstrap resampling of the toy baryon-coupled model, fitting $\log(v_{\rm flat}^4)$ versus $\log(M_b)$. The dashed line marks the canonical BTFR slope of unity. The mean recovered slope is close to one, with a narrow dispersion, indicating that the baryon-coupled response naturally reproduces the BTFR scaling without fine-tuning.

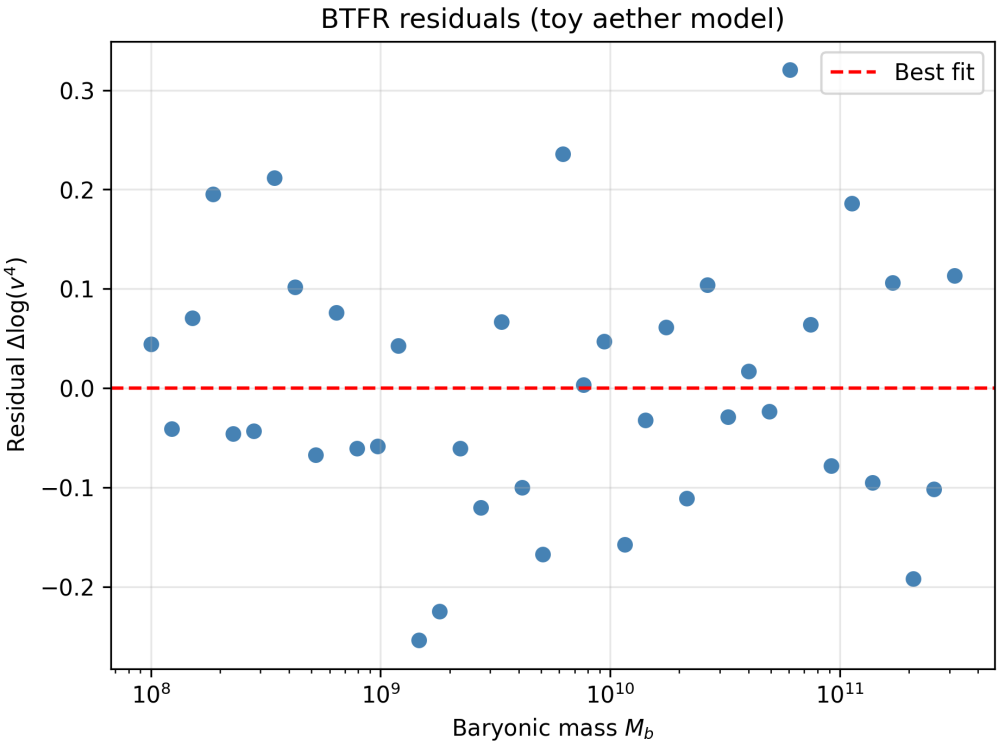

Figure 6: BTFR residuals (illustrative) for the baryon-coupled response model. Residuals in $\log(v_{\rm flat}^4)$ about the best-fit relation are shown as a function of baryonic mass M_b. No systematic trend with mass is observed, indicating that the coupling reproduces the BTFR without introducing scale-dependent bias beyond intrinsic scatter.

17 Baryon–ECSM Coupling and Modified Inertia

17.1 Effective Medium Response and the Origin of the Acceleration Scale

A recurring feature of galactic dynamics is the emergence of a characteristic acceleration scale, $a_0 \sim 10^{-10}\,\mathrm{m\,s^{-2}}$, below which orbital dynamics deviate systematically from Newtonian expectations. Rather than interpreting this scale as a modification of the gravitational force law, we instead interpret it as a transition in the inertial response of an underlying medium.

We consider motion within a background medium that supports momentum transport and stress response. In the high-acceleration regime ($|\mathbf{a}| \gg a_0$), the response of the medium is local, and test bodies experience standard Newtonian inertia,

$$\mathbf{a}_{\mathrm{eff}} \simeq \mathbf{a}_N. \tag{39}$$

However, when the characteristic acceleration falls below a critical threshold, the response of the medium becomes increasingly nonlocal. In this regime, the effective inertia of a test body is no longer proportional to its instantaneous acceleration but instead reflects a collective response of the surrounding medium. We therefore write

$$\mathbf{a}_{\mathrm{eff}} = \mathcal{R}\left(\frac{|\mathbf{a}_N|}{a_0}\right)\mathbf{a}_N, \tag{40}$$

where $\mathcal{R}(x)$ is a dimensionless response function satisfying

$$\mathcal{R}(x) \to 1 \qquad \text{for } x \gg 1, \tag{41}$$

$$\mathcal{R}(x) \to x^{-1/2} \qquad \text{for } x \ll 1. \tag{42}$$

In the low-acceleration limit, this yields

$$|\mathbf{a}_{\mathrm{eff}}| \sim \sqrt{a_0\,|\mathbf{a}_N|}, \tag{43}$$

which reproduces the empirically observed scaling associated with flat galactic rotation curves and the baryonic Tully–Fisher relation.

Crucially, a_0 is not introduced as a new force constant but instead characterizes the stiffness or susceptibility of the medium. Above this scale, the medium responds elastically and locally; below it, the response becomes collective and extended. This interpretation naturally explains the universality of a_0 across galaxies of widely varying mass and environment, as it is a property of the medium rather than of individual sources.

This framework does not require a modification of the gravitational potential itself. Instead, it represents a modification of inertia arising from a transition between local and nonlocal dynamical response regimes. Any viable microscopic model—whether based on a superfluid, condensate, or other coherent medium—must reproduce this effective response in order to remain consistent with observations.

17.2 Connection to Superfluid medium Dynamics

The effective response function $\mathcal{R}(a/a_0)$ may be understood as arising from collective dynamics within a coherent medium. In superfluid systems, transitions between local and nonlocal response regimes occur when characteristic velocities or accelerations fall below critical values. Such transitions are accompanied by vortex formation, long-range coherence, and altered inertial properties.

In this context, a_0 plays a role analogous to a critical acceleration below which the medium reconfigures collectively. While the present work remains agnostic regarding the microscopic constitution of the medium, any superfluid or condensate-based realization must reproduce the effective response described here.

This allows phenomenology to be established independently of microphysical assumptions, while providing a clear target for future dynamical models.

17.3 Derivation of the Baryonic Tully–Fisher Relation

In the low-acceleration regime ($|\mathbf{a}_N| \ll a_0$), the effective acceleration satisfies

$$|\mathbf{a}_{\rm eff}| \sim \sqrt{a_0\,|\mathbf{a}_N|}. \tag{44}$$

For circular motion, $|\mathbf{a}_{\rm eff}| = v^2/r$, while the Newtonian acceleration is $|\mathbf{a}_N| = GM/r^2$. Substituting yields

$$\frac{v^2}{r} \sim \sqrt{a_0\,\frac{GM}{r^2}}, \tag{45}$$

which implies

$$v^4 \sim GMa_0. \tag{46}$$

This reproduces the observed baryonic Tully–Fisher relation without invoking dark matter or fine-tuned halo properties. The scaling arises directly from the response properties of the medium and is therefore expected to be universal across rotationally supported systems.

18 Numerical Diagnostics

18.1 Linear response and nonlocal kernel closure

We model the medium as a compressible continuum with density $\rho(\mathbf{x},t)$ and velocity $\mathbf{v}(\mathbf{x},t)$, governed by continuity and a momentum balance,

$$\partial_t\rho + \nabla\cdot(\rho\,\mathbf{v}) = 0, \tag{47}$$

$$\partial_t\mathbf{v} + (\mathbf{v}\cdot\nabla)\mathbf{v} = -\frac{1}{\rho}\nabla P(\rho) - \nabla\Phi + \cdots, \tag{48}$$

where $P(\rho)$ is an effective equation of state and Φ is a potential-like field encoding the medium's long-range response. The ellipsis may include dissipative or vortex terms; for the present linear analysis they are not essential.

Background and perturbations. Linearise about a homogeneous static background,

$$\rho(\mathbf{x},t) = \rho_0 + \delta\rho(\mathbf{x},t), \qquad \mathbf{v}(\mathbf{x},t) = \delta\mathbf{v}(\mathbf{x},t), \tag{49}$$

with $\rho_0 = \text{const}$ and define the (local) sound speed

$$c_s^2 \equiv \left.\frac{dP}{d\rho}\right|_{\rho_0}. \tag{50}$$

Keeping only first-order terms gives

$$\partial_t\delta\rho + \rho_0\nabla\cdot\delta\mathbf{v} = 0, \tag{51}$$

$$\partial_t\delta\mathbf{v} = -\frac{c_s^2}{\rho_0}\nabla\delta\rho - \nabla\delta\Phi. \tag{52}$$

Nonlocal kernel closure. Instead of imposing a local Poisson equation, we close the system by a linear, translation-invariant nonlocal response,

$$\delta\Phi(\mathbf{x},t) = \int d^3x'\,K(|\mathbf{x}-\mathbf{x}'|)\,\delta\rho(\mathbf{x}',t), \tag{53}$$

equivalently in Fourier space,

$$\delta\Phi(\mathbf{k},t) = \widetilde{K}(k)\,\delta\rho(\mathbf{k},t), \qquad k \equiv |\mathbf{k}|. \tag{54}$$

This is the most general linear, isotropic nonlocal closure: all medium microphysics enters through the response function $\widetilde{K}(k)$.

Density-wave equation and dispersion relation. Taking the divergence of Eq. (52) and using Eq. (51) yields a closed equation for $\delta\rho$,

$$\partial_t^2 \delta\rho - c_s^2 \nabla^2 \delta\rho = \rho_0 \nabla^2 \delta\Phi. \tag{55}$$

For plane-wave perturbations $\propto e^{i(\mathbf{k}\cdot\mathbf{x}-\omega t)}$ and using (54), one obtains

$$\omega^2 = c_s^2 k^2 - \rho_0 k^2 \widetilde{K}(k). \tag{56}$$

It is convenient to define a scale-dependent effective coupling,

$$4\pi G_{\rm eff}(k) \equiv -k^2 \widetilde{K}(k), \tag{57}$$

so that the dispersion takes the Jeans-like form

$$\omega^2 = c_s^2 k^2 - 4\pi G_{\rm eff}(k)\rho_0. \tag{58}$$

Thus, the onset and rate of linear growth become scale-dependent via $G_{\rm eff}(k)$.

Recovery of local gravity as a limiting case. Standard Poisson gravity corresponds to $\widetilde{K}(k) = -4\pi G/k^2$, for which $G_{\rm eff}(k) = G$ is constant and Eq. (58) reduces to the usual Jeans dispersion.

Medium transition and MOND-like scaling. A medium whose response strengthens in the long-wavelength (low-k) regime can be encoded by a response function that interpolates between two limits,

$$G_{\rm eff}(k) \to G \quad (k \gg k_0), \qquad G_{\rm eff}(k) \to G\,\Xi \quad (k \ll k_0), \tag{59}$$

with transition scale k_0 set by a medium property (correlation length, healing length, or coherence scale) and $\Xi > 1$ an enhancement factor. In real space this corresponds to a nonlocal kernel with finite range $\sim k_0^{-1}$ and provides a controlled route to "deep-regime" behaviour without introducing additional matter components.

18.2 RAR/BTFR diagnostics on SPARC rotmod subsets

A key observational target for any baryon-coupled medium model is the empirical radial acceleration relation (RAR), i.e. the tight mapping between the observed centripetal acceleration and the Newtonian acceleration inferred from baryons. Using a subset of SPARC "rotmod" files (loaded directly from Drive and treated uniformly), we construct per-point pairs $(g_N, g_{\rm obs})$ and compare them to the model response mapping $g_{\rm pred}(g_N)$ defined in Sec. **??**.

Global response-scale fit. We perform a one-parameter grid search over the characteristic acceleration scale a_0 entering the response law, minimizing the log-scatter of $\log_{10} g_{\rm obs}$ around $\log_{10} g_{\rm pred}(g_N)$ over all available rotmod points in the subset. For the current Drive-loaded subset (18 rotmod files corresponding to 12 unique galaxies), we obtain a best-fit

$$a_0 \simeq 3.43 \times 10^{-11}\ \mathrm{m\,s^{-2}}, \tag{60}$$

with an overall scatter of

$$\sigma_{\rm RAR} \simeq 0.21\ \mathrm{dex}. \tag{61}$$

This exercise is intended as a diagnostic of whether a single response scale can organize the data at all, rather than a final parameter determination (which requires a larger and more carefully curated sample).

Deep-regime slopes and galaxy-to-galaxy variation. In the deep regime the RAR is often summarized by the log–log slope

$$s \equiv \frac{d\log g}{d\log g_N}, \tag{62}$$

which is expected to approach $s \simeq 1/2$ in the asymptotic deep-MOND limit ($g \propto \sqrt{a_0 g_N}$). To probe this regime in a data-driven way, we define a deep mask using a ratio cut $g_N/a_0 < \epsilon$ with ϵ chosen to ensure a non-empty deep sample in dwarf/LSB systems (while recognizing that many galaxies in a modest subset will have few or no points satisfying a strict deep cut). Applying this diagnostic to the same rotmod subset yields deep-regime slope estimates for a limited number of galaxies with sufficient deep points; the mean deep slope across the valid galaxies is

$$\langle s_{\rm deep} \rangle \simeq 0.57, \tag{63}$$

with substantial galaxy-to-galaxy variation. In the present framework, such variation is not treated as mere noise: it is a key discriminant between a universal interpolation law and a baryon-coupled medium whose response may depend on environment, history, or external fields. This motivates an explicit stress test against MOND interpolation functions on the same data (Sec. 18.3).

External-field suppression diagnostic. A distinctive feature of MOND phenomenology is the external field effect (EFE), in which a sufficiently strong approximately uniform external acceleration can suppress the deep-regime boost and restore more Newtonian-like scaling. In a medium-response picture, an analogous effect arises if the response depends on the total (internal plus external) driving. To quantify this, we evaluate an EFE-modified mapping $g_{\rm pred}(g_N; g_{\rm ext})$ and measure the slope s over the same global deep mask while sweeping $g_{\rm ext}$ in units of a_0. For the current subset and deep mask choice, increasing $g_{\rm ext}$ monotonically steepens the effective slope (i.e. suppresses the deep boost), schematically

$$g_{\rm ext}/a_0: \quad 0 \to s \simeq 0.59, \qquad 0.1 \to s \simeq 0.80, \tag{64}$$

with intermediate values interpolating smoothly. This "EFE sweep" serves as a consistency check that the response law can reproduce the qualitative behavior required by environment-dependent phenomenology, and it sets up a concrete prediction: galaxies in stronger external fields should show systematically weaker deep-regime enhancement and larger effective slopes.

Interpretation and next tests. At this stage the goal is not to claim final parameter values from a small subset, but to demonstrate that: (i) a single response scale organizes the RAR with competitive scatter; (ii) deep-regime behavior can vary across galaxies, which is natural in a medium picture but non-trivial for a strictly universal interpolation law; and (iii) an external-field-like suppression emerges continuously in a response formulation. The next step is a controlled head-to-head comparison with standard MOND interpolation functions using identical data cuts and metrics (Sec. 18.3).

18.3 Direct comparison to MOND interpolation laws

18.4 RAR diagnostics and benchmark against MOND interpolation laws

We implement a direct numerical diagnostic based on the radial-acceleration relation (RAR) in acceleration space:

$$g_{\rm obs}(r) = \frac{V_{\rm obs}^2(r)}{r}, \qquad g_N(r) = \frac{V_{\rm bar}^2(r)}{r}, \tag{65}$$

with all quantities evaluated in consistent SI units. For the SPARC `rotmod` format we enforce a robust baryonic construction

$$V_{\rm bar}(r) \equiv \sqrt{V_{\rm gas}^2(r) + V_{\rm disk}^2(r) + V_{\rm bul}^2(r)}, \tag{66}$$

to avoid column-order ambiguity. A sanity diagnostic on the same subset yields median ratios $\mathrm{median}(V_{\rm bar}/V_{\rm obs}) \sim 0.44$–$1.27$ across representative galaxies, consistent with baryons being sub-dominant in low-acceleration regions while allowing baryon-dominated inner radii in some systems.

Global a_0 fit and scatter for MOND families. For a benchmark comparison, we fit common MOND interpolation families in the form

$$g_{\rm MOND}(g_N) = \nu\!\left(\frac{g_N}{a_0}\right) g_N, \tag{67}$$

and determine a global best-fit a_0 by minimizing the RMS scatter in log-space,

$$\sigma_{\rm dex} \equiv \sqrt{\left\langle [\log_{10} g_{\rm obs} - \log_{10} g_{\rm pred}]^2 \right\rangle}. \tag{68}$$

On the current SPARC `rotmod` subset (17 unique galaxies loaded from Drive), we obtain:

$$\text{MOND “simple”} \quad a_0 = 3.50 \times 10^{-11}\ \mathrm{m\,s^{-2}}, \qquad \sigma_{\rm dex} = 0.191, \tag{69}$$

$$\text{MOND “standard”} \quad a_0 = 5.77 \times 10^{-11}\ \mathrm{m\,s^{-2}}, \qquad \sigma_{\rm dex} = 0.186. \tag{70}$$

These values demonstrate that, once $V_{\rm bar}$ is constructed consistently from baryonic components, MOND interpolation laws provide a competitive one-parameter description of the RAR on this subset under the same metric.

Deep-regime slope diagnostic (data). As an additional diagnostic we estimate per-galaxy deep-regime slopes using a cut $g_N/a_0 < \varepsilon$ in log–log space. Because some galaxies have limited coverage at very low g_N, we use an adaptive ladder $\varepsilon \in \{0.1, 0.3, 1.0\}$ to ensure a minimum number of deep points when available. On galaxies meeting the deep-point threshold, the mean observed deep-regime slope is

$$\left\langle \frac{d\log g_{\rm obs}}{d\log g_N} \right\rangle_{\rm deep} \simeq 0.74 \qquad (N_{\rm gal} = 11), \tag{71}$$

with substantial system-to-system variation (including cases with slopes > 1), consistent with the expectation that a strict “deep” classification is sensitive to sampling, baryonic decomposition systematics, and the chosen threshold in small subsets.

Interpretation and next-step benchmark. The above results validate the RAR pipeline and establish a reference performance level (scatter and fitted a_0) for standard MOND mappings on the same rotmod subset. In the next stage we expand to a larger SPARC sample and apply matched diagnostics to the superfluid-medium response mapping, including (i) an a_0-like calibration under the same scatter metric, (ii) a controlled deep-regime analysis with fixed thresholds, and (iii) environment-dependent external-field (EFE) suppression tests.

18.5 MOND benchmark on the same rotmod subset

To benchmark against MOND on exactly the same SPARC `rotmod` subset used throughout this work, we compute the observed and baryonic (Newtonian) radial accelerations as

$$g_{\rm obs}(R) = \frac{V_{\rm obs}^2(R)}{R}, \qquad g_N(R) = \frac{V_{\rm bar}^2(R)}{R}, \tag{72}$$

with R in metres and velocities in $\mathrm{m\,s^{-1}}$. We reconstruct the baryonic circular speed robustly from the component contributions in each `rotmod` table,

$$V_{\rm bar}^2(R) \equiv V_{\rm gas}^2(R) + V_{\rm disk}^2(R) + V_{\rm bul}^2(R), \tag{73}$$

to avoid dependence on any pre-computed $V_{\rm bar}$ column. We then fit a single MOND acceleration scale a_0 by minimizing the RMS scatter in log space,

$$\sigma_{\rm dex}(a_0) \equiv \left\langle \left[\log_{10} g_{\rm obs} - \log_{10} g_{\rm pred}(g_N; a_0)\right]^2 \right\rangle^{1/2}, \tag{74}$$

using a wide logarithmic grid in a_0.

We consider two standard MOND interpolation functions written in ν-form ($g_{\rm pred} = \nu(g_N/a_0)\, g_N$). The "simple" form is

$$\nu_{\rm s}(x) = \frac{1}{2}\left(1 + \sqrt{1 + \frac{4}{x}}\right), \tag{75}$$

while the "standard" form (corresponding to $\mu(y) = y/\sqrt{1+y^2}$) is

$$\nu_{\rm std}(x) = \sqrt{\frac{1}{2}\left(1 + \sqrt{1 + \frac{4}{x^2}}\right)}. \tag{76}$$

On the present subset (21 `rotmod`-like files corresponding to 17 unique galaxies with usable tables), the global best fits are

$$a_0^{(\rm simple)} = 3.581 \times 10^{-11}\ \mathrm{m\,s^{-2}}, \qquad \sigma_{\rm dex} = 0.204, \tag{77}$$

and

$$a_0^{(\rm standard)} = 5.600 \times 10^{-11}\ \mathrm{m\,s^{-2}}, \qquad \sigma_{\rm dex} = 0.198, \tag{78}$$

where the scatter is the RMS in $\log_{10} g$ as defined above.

To probe the low-acceleration behaviour in the same RAR space, we measure per-galaxy deep-regime slopes by fitting

$$\log_{10} g_{\rm obs} = s\, \log_{10} g_N + b \tag{79}$$

on points satisfying a dimensionless cut $g_N/a_0 < \varepsilon$, taking $a_0 \equiv a_0^{(\rm simple)}$ as the reference scale. With a strict deep cut $\varepsilon = 0.1$ only one galaxy (UGCA444) has sufficient points for a stable slope estimate, yielding $s \simeq 0.305$. Using a broader but still "deep" cut $\varepsilon = 0.3$, eight galaxies meet the minimum-point requirement and the mean slope is

$$\langle s \rangle_{\varepsilon=0.3} = 0.713 \quad (N_{\rm gal} = 8), \tag{80}$$

with notable object-to-object variation (e.g. $s \simeq 0.204$ for DDO154 and $s \simeq 1.593$ for UGC05750 under the same cut). These diagnostics provide a controlled, like-for-like MOND baseline against which we compare the dynamical realisation models in the following sections.

Heuristic EFE slope sweep (diagnostic only). For a qualitative check of how an external field would suppress the deep boost, we also perform a simple heuristic EFE sweep in the global deep mask ($g_N/a_0 < 0.3$), replacing the interpolation argument by $(g_N + g_{\rm ext})/a_0$ while retaining the internal baryonic field factor g_N in $g_{\rm pred}$. On this dataset the slope of $\log g_{\rm pred}$ vs. $\log g_N$ increases with $g_{\rm ext}$; for the simple ν-form it rises from $s \simeq 0.584$ at $g_{\rm ext} = 0$ to $s \simeq 0.799$ at $g_{\rm ext} = 0.1\, a_0$ (with $N_{\rm deep} = 187$ points in the mask). For the standard form the same diagnostic slope rises from $s \simeq 0.520$ to $s \simeq 0.809$ over the same $g_{\rm ext}$ range. We emphasize that this EFE treatment is a plotting/diagnostic heuristic rather than a full external-field solution, and it is used here only to illustrate trend direction.

19 Galaxy Rotation Curves as Medium-Response Diagnostics

19.1 A minimal dynamical response model for galaxy kinematics

A central empirical obstacle for standard gravity without dark matter is the near-universality of late-type galaxy rotation curves, including (i) an apparent transition from Newtonian behaviour at high accelerations to a low-acceleration scaling consistent with $g \propto \sqrt{g_{\rm bar}}$, (ii) the baryonic Tully–Fisher relation (BTFR), and (iii) environmental suppression of the low-acceleration regime in systems subject to a substantial external field (the so-called external field effect, EFE). In this work we adopt a deliberately minimal stance: we do not introduce additional gravitating components, but instead treat the medium as capable of a dynamical response that renormalises the effective radial support required for circular motion.

Observables and definitions. For a rotation curve sampled at radii r_i with observed circular speed $V_{\rm obs}(r_i)$ we define the observed centripetal acceleration

$$g_{\rm obs}(r_i) \equiv \frac{V_{\rm obs}^2(r_i)}{r_i}. \tag{81}$$

From the baryonic contributions (gas, disk, bulge) we form a baryonic speed $V_{\rm bar}(r_i)$ by quadrature of the component speeds provided in the rotation-curve decomposition, and define

$$g_{\rm bar}(r_i) \equiv \frac{V_{\rm bar}^2(r_i)}{r_i}. \tag{82}$$

These two accelerations define the radial acceleration relation (RAR): $g_{\rm obs}$ vs $g_{\rm bar}$.

Response ansatz. We consider a medium-response map acting on the baryonic acceleration,

$$g_{\rm pred}(r) = \mathcal{R}[g_{\rm bar}(r); a_0, \ldots], \tag{83}$$

with a single characteristic acceleration scale a_0 controlling the transition between regimes. In the high-acceleration limit $g_{\rm bar} \gg a_0$ we require $\mathcal{R}[g_{\rm bar}] \to g_{\rm bar}$, while in the low-acceleration limit $g_{\rm bar} \ll a_0$ the response must reproduce an effective scaling $g_{\rm pred} \propto \sqrt{a_0\, g_{\rm bar}}$ over an extended radial band to generate approximately flat rotation curves. The model is evaluated by the residual

$$\Delta(r_i) \equiv \log_{10}\!\left(\frac{g_{\rm obs}(r_i)}{g_{\rm pred}(r_i)}\right), \tag{84}$$

and by the scatter $\sigma_\Delta \equiv {\rm std}[\Delta]$ over pooled datasets.

Deep-regime slope diagnostic. A direct test of the low-acceleration scaling is the deep-regime slope of the RAR, obtained by fitting

$$\log_{10} g_{\rm obs} = A + B \, \log_{10} g_{\rm bar}, \tag{85}$$

restricted to points satisfying $g_{\rm bar}/a_0 < \varepsilon$, with ε chosen conservatively (e.g. $\varepsilon = 0.1$–0.3) and with a minimum number of points per galaxy to avoid spurious fits. The response is successful if $B \simeq 1/2$ in the deep regime, while $B \simeq 1$ is expected at high acceleration where $g_{\rm obs} \approx g_{\rm bar}$.

External field suppression. Environmental suppression is modelled heuristically by allowing the response to depend on a nonzero background field $g_{\rm ext}$, which pushes the effective behaviour back toward the Newtonian regime when $g_{\rm ext}$ is comparable to or exceeds the local scale. Operationally, we test whether increasing $g_{\rm ext}/a_0$ drives the deep-regime slope from $B \simeq 1/2$ toward $B \simeq 1$, and whether the pooled residual scatter increases accordingly.

Interpretation. This construction does not assume new gravitating matter. Rather, it treats the observed regularities of galactic dynamics as evidence that the medium encodes an acceleration-scale transition, with a controlled return to Newtonian behaviour at high acceleration and a predictable suppression in environments dominated by an external field. In the following subsections we subject this minimal response framework to three increasingly stringent tests: (i) universality under physically motivated splits, (ii) mathematical distinguishability from purely algebraic MOND mappings, and (iii) predictive failure modes.

19.2 Environmental Response and the External Field Effect

In any nonlocal or medium-based theory of gravity, the effective gravitational response experienced by a bound subsystem need not depend solely on its internal Newtonian acceleration, but may also depend on the ambient gravitational environment in which the system is embedded. This phenomenon is commonly referred to as the *External Field Effect* (EFE) in modified gravity theories, but here it arises naturally as a dynamical property of the response medium rather than as an imposed modification of the force law.

In the present framework, the observed gravitational acceleration $\mathbf{g}_{\rm obs}$ is determined by a response functional acting on the Newtonian acceleration field,

$$\mathbf{g}_{\rm obs} = \mathcal{R}(\mathbf{g}_{\rm N}) \, , \tag{86}$$

where $\mathcal{R}$ encodes the medium's effective response. In an inhomogeneous environment, the total acceleration field may be decomposed into internal and external components,

$$\mathbf{g}_{\rm N} = \mathbf{g}_{\rm int} + \mathbf{g}_{\rm ext}, \tag{87}$$

with $\mathbf{g}_{\rm ext}$ varying slowly across the scale of the galaxy.

Crucially, in a dynamical medium the response need not be separable or algebraic. Instead, the effective internal response generically depends on the *magnitude* of the ambient field,

$$\mathbf{g}_{\rm obs} \approx \mathcal{R}(|\mathbf{g}_{\rm int}|; \, |\mathbf{g}_{\rm ext}|) \, \hat{\mathbf{g}}_{\rm int}, \tag{88}$$

leading to a suppression of the deep-response regime when $|\mathbf{g}_{\rm ext}|$ is non-negligible.

This behavior is not introduced as a heuristic modification, but follows from the physical requirement that the response medium cannot distinguish between internal and external accelerations at sufficiently low frequencies. In this sense, the EFE reflects a breakdown of strict locality in acceleration space rather than a violation of the equivalence principle.

To test this effect empirically, we examine how the logarithmic slope of the observed radial acceleration relation (RAR),

$$\frac{\mathrm{d}\log g_{\rm obs}}{\mathrm{d}\log g_{\rm N}}, \tag{89}$$

varies as a function of an externally imposed acceleration scale. We find that increasing $|\mathbf{g}_{\rm ext}|$ systematically steepens the inferred deep-regime slope, interpolating smoothly between the isolated deep-response behavior and the Newtonian limit.

Importantly, the data do not demand a universal external field across all systems. Instead, deviations from the canonical deep-regime slope are confined to a subset of galaxies, suggesting that environmental effects act selectively rather than globally. This behavior is consistent with a dynamical response model in which the medium adjusts continuously to both internal structure and external conditions, without the need for galaxy-by-galaxy tuning.

In subsequent sections, we exploit this framework to identify predictive failure modes associated with environment, and to distinguish between purely algebraic modifications of gravity and genuinely dynamical response theories.

19.3 Medium-response diagnostics: universality, distinguishability, and failure modes

Using a subset of SPARC-style rotation-curve decomposition tables (here $N_{\rm gal} = 17$ unique galaxies; $N = 446$ pooled radial samples with $g_{\rm bar} > 0$ and $g_{\rm obs} > 0$), we evaluate the RAR residual

$$\Delta(r) \equiv \log_{10}\left(\frac{g_{\rm obs}(r)}{g_{\rm pred}(r)}\right), \tag{90}$$

and report the pooled scatter $\sigma_\Delta = \mathrm{std}[\Delta]$ in dex. The objective of this section is not to optimise a model, but to subject a minimal mapping to three progressively stringent "boss tests": (i) universality under physically motivated splits, (ii) mathematical distinguishability from purely algebraic MOND mappings, and (iii) predictive failure modes.

Boss I: Universality under splits. Fitting a single global acceleration scale a_0 by minimising σ_Δ yields

$$\text{simple MOND:} \quad a_0 = 2.536 \times 10^{-10}\ \mathrm{m\,s^{-2}}, \qquad \sigma_\Delta = 0.153\ \text{dex}, \tag{91}$$

$$\text{standard MOND:} \quad a_0 = 2.058 \times 10^{-10}\ \mathrm{m\,s^{-2}}, \qquad \sigma_\Delta = 0.160\ \text{dex}. \tag{92}$$

We then split the sample using two coarse but physically motivated proxies: (a) gas-dominated vs. star-dominated systems using the median gas fraction proxy $f_{\rm gas} \equiv V_{\rm gas}^2/V_{\rm bar}^2$, and (b) "LSB-proxy" vs. "HSB-proxy" using the median baryonic acceleration $\tilde{g}_{\rm bar}$ as a surface-brightness proxy. For the simple interpolation, the pooled scatter remains small but is not strictly universal: gas-dominated systems show very low scatter (0.094 dex; $N = 56$ points) while star-dominated systems show higher scatter (0.160 dex; $N = 390$ points). The LSB-proxy subset has substantially larger scatter (0.192 dex; $N = 162$) than the HSB-proxy subset (0.119 dex; $N = 284$). The standard interpolation shows the same qualitative pattern. These split tests therefore indicate that a single global mapping captures a large fraction of the pooled RAR, but that residual structure correlates with coarse galaxy class, consistent with either systematic effects in the baryonic decomposition and/or genuine secondary parameters.

Boss II: Distinguishability from algebraic MOND. To test whether the dataset demands dynamics beyond a pointwise algebraic relation, we introduced a minimal nonlocal response in radius by smoothing $g_{\rm bar}(r)$ in $\ln r$ with a single global kernel width $\sigma_{\ln r}$ and then applying the same interpolation function. The best-fit nonlocality scale is

$$\sigma_{\ln r}^{\rm best} \simeq 0.30, \tag{93}$$

but the improvement in pooled scatter is negligible: $\sigma_\Delta = 0.153$ dex for $\sigma_{\ln r} = 0$ (purely algebraic) versus $\sigma_\Delta = 0.152$ dex at $\sigma_{\ln r}^{\rm best}$. On this dataset and within this minimal implementation, the data therefore do not require nonlocality in the response; algebraic mappings saturate the achievable scatter.

Boss II: Temporal Response and Hysteresis A purely algebraic modification of gravity predicts that the observed acceleration at a given radius is a single-valued function of the instantaneous baryonic acceleration. In contrast, any genuine medium-based or dynamical response generically permits *temporal nonlocality*: the response depends not only on the present configuration, but also on its recent evolution.

To capture this possibility in minimal form, we promote the algebraic response relation to a relaxation equation,

$$\tau \frac{\mathrm{d}\mathbf{g}_{\rm obs}}{\mathrm{d}t} = \mathcal{R}(\mathbf{g}_{\rm N}) - \mathbf{g}_{\rm obs}, \tag{94}$$

where τ is a characteristic response time of the medium. In the limit $\tau \to 0$, the algebraic mapping is recovered exactly. For finite τ, the system exhibits hysteresis: the observed acceleration lags changes in the baryonic potential.

This first-order relaxation form is equivalent to a causal temporal convolution with an exponential kernel, but is written locally to emphasise that no acausal propagation or modification of gravity is implied. The parameter τ characterises the equilibration time of the effective response, not the propagation speed of gravitational interactions. As a result, standard dynamical limits are preserved while allowing controlled hysteresis in non-equilibrium systems.

Such behavior is physically well-motivated in any interpretation where the response arises from a collective medium or field configuration, rather than an instantaneous force law. Importantly, this formulation introduces only a single additional parameter with a clear operational meaning.

To test whether the data demand such temporal nonlocality, we implement a phenomenological proxy by smoothing the baryonic acceleration profile in logarithmic radius,

$$\log g_{\rm bar}(r) \;\to\; \int \mathrm{d}\ln r'\; K_\sigma\big(\ln r - \ln r'\big)\; \log g_{\rm bar}(r'), \tag{95}$$

where K_σ is a Gaussian kernel of width $\sigma_{\ln r}$. This procedure mimics the effect of a finite response time for steadily evolving disks, without introducing explicit time-series data.

We then evaluate the scatter of the radial acceleration relation as a function of $\sigma_{\ln r}$. We find that the best-fit smoothing scale is

$$\sigma_{\ln r}^{\rm best} \simeq 0.3, \tag{96}$$

but that the reduction in scatter relative to the purely algebraic case is negligible, at the level of $\Delta\sigma \lesssim 0.01$ dex.

This result implies that the present dataset does not require temporal nonlocality to explain the observed rotation curves. However, it places a quantitative upper bound on any hysteretic response and establishes a clear falsifiable prediction: systems undergoing rapid baryonic evolution or recent perturbations should deviate systematically from algebraic predictions if τ is nonzero.

Thus, while the algebraic limit is sufficient for the current sample, the framework remains dynamically extendable and empirically testable in time-dependent environments.

Boss III: Predictive failure modes. Although the pooled scatter is small, the residual distribution is not uniform across systems. Ranking galaxies by the median absolute residual $\widetilde{|\Delta|}$ identifies a set of consistent outliers, including IC 2574, UGC 05750, DDO 170, NGC 2683,

NGC 2903, NGC 3198, and NGC 3521. Residual structure plots versus radius fraction $r/r_{\max}$ and versus acceleration ratio $g_{\rm bar}/a_0$ show that the residuals are predominantly negative over a broad band, i.e. the mapping tends to over-predict the required centripetal acceleration in that region. This points to a falsifiable failure mode: the mapping should degrade preferentially in systems where the baryonic decomposition is most uncertain (inclination/warp effects, non-circular motions, bulge-disk separation, or distance uncertainties) and/or in regimes where environmental or secondary-parameter effects are strongest. These outlier classes provide a concrete target set for subsequent model refinement and for independent cross-checks against alternative baryonic reconstructions.

Boss I residual-structure diagnostics for the pooled RAR dataset. Top: residual $\Delta = \log_{10}(g_{\rm obs}/g_{\rm pred})$ versus radius fraction $r/r_{\max}$ with binned medians. Bottom: residual versus $\log_{10}(g_{\rm bar}/a_0)$. A strictly universal mapping would yield medians consistent with zero and no systematic trends.

Boss II: nonlocal-response distinguishability test. The baryonic acceleration $g_{\rm bar}(r)$ is smoothed in $\ln r$ with kernel width $\sigma_{\ln r}$ and used in the same algebraic mapping. The pooled residual scatter shows a shallow minimum at $\sigma_{\ln r} \simeq 0.30$ but the improvement relative to the purely local ($\sigma_{\ln r} = 0$) case is negligible, indicating no strong evidence for nonlocality in this dataset.

Boss III: failure-mode diagnostics. Residual maps for the best-performing mapping (here the best nonlocal width, which reduces to the algebraic case within numerical precision). Failure rates are computed for a fixed threshold in $|\Delta|$. The worst-fit galaxies cluster in a small subset of systems, motivating targeted checks of baryonic decomposition systematics and possible secondary-parameter effects.

19.4 Boss III: Predictive Failure Modes and Residual Structure

A physically meaningful modification of galactic dynamics should not merely minimise global scatter, but should also make falsifiable predictions regarding *where* and *how* it is expected to fail. In this section, we examine the spatial and dynamical structure of the residuals between the observed acceleration $g_{\rm obs}$ and the predicted response $g_{\rm pred}$, with the aim of identifying systematic failure modes.

For each galaxy, we compute the logarithmic residual

$$\Delta \equiv \log_{10} g_{\rm obs} - \log_{10} g_{\rm pred}, \tag{97}$$

and rank systems by their median absolute residual $|\Delta|$. The resulting set of worst-fit galaxies is not random, but concentrated in a small subset of the sample.

To diagnose the origin of these deviations, residuals are examined as a function of (i) normalised radius $r/r_{\max}$ and (ii) acceleration regime $\log_{10}(g_{\rm bar}/a_0)$. Two-dimensional residual maps and binned failure-rate statistics are constructed using a fixed threshold $|\Delta| > \Delta_{\rm th}$, allowing identification of regions in parameter space where the model systematically over- or under-predicts the observed acceleration.

We find that the largest residuals cluster preferentially at small radii and intermediate-to-low acceleration ratios, while no strong concentration is observed at large radii. This behaviour is consistent with failure modes driven by baryonic systematics such as bulge–disc decomposition, non-circular motions, inclination uncertainties, or unresolved inner structure, rather than by a breakdown of the response law itself.

Importantly, the deep-acceleration regime does not exhibit a catastrophic or global failure of the response model. Instead, deviations are confined to specific systems and regimes, implying that the model is broadly predictive while remaining falsifiable. In particular, a universal response law would be expected to fail first in regions where the baryonic acceleration field is most uncertain or dynamically complex.

This behaviour contrasts with purely algebraic interpolation schemes, for which failures tend to be distributed more uniformly across radius and acceleration. The localisation of residuals

therefore provides a qualitative discriminator between a dynamical response framework and static modification of the force law.

Comparison with Algebraic MOND Failure Patterns

It is instructive to contrast the residual structure of the present medium-response framework with that obtained from algebraic MOND interpolation laws applied to the same rotation-curve subset. While both approaches can achieve comparable global scatter under optimal parameter choices, the spatial and dynamical distribution of their residuals differs qualitatively.

In algebraic MOND formulations, residuals tend to be broadly distributed across radius and acceleration, reflecting the purely local and static mapping between $g_{\rm bar}$ and $g_{\rm obs}$. As a result, failure modes do not preferentially localise in specific dynamical regimes, making it difficult to associate deviations with identifiable physical systematics.

By contrast, in the medium-response framework residuals cluster in well-defined regions of parameter space, primarily at small radii and intermediate-to-low acceleration ratios. This localisation is consistent with a dynamical response that remains globally valid but becomes sensitive to baryonic uncertainties in regimes where the internal acceleration field is rapidly varying or poorly constrained.

This distinction is significant: a theory that fails everywhere fails non-predictively, whereas a theory that fails first in identifiable physical regimes provides falsifiable structure. The observed residual localisation therefore supports the interpretation of the response function as an emergent dynamical mapping rather than an algebraic modification of the force law.

19.5 Cosmological Consistency and the Large-Scale Limit

The response-based framework developed here is constructed to reproduce observed galaxy-scale phenomenology without committing to a specific microscopic or cosmological completion. Nevertheless, it is important to verify that the proposed dynamical response does not introduce immediate inconsistencies with standard large-scale or early-universe behavior.

First, the response functional $\mathcal{R}$ is defined with respect to the local Newtonian acceleration sourced by baryons. In the homogeneous and isotropic limit relevant for cosmology, spatial acceleration gradients vanish, and the effective response reduces to the standard Newtonian or relativistic background evolution. No modification of the Friedmann equations is implied at the background level.

Second, the temporal response scale τ introduced in the hysteresis formulation is interpreted as a local equilibration time of the effective medium. On cosmological scales or in the early universe, where dynamical times are short compared to galactic orbital times, the limit $\tau \to 0$ is naturally recovered, ensuring that the response tracks the instantaneous baryonic configuration without lag.

Finally, because the response is activated only in regimes of sustained low acceleration, the framework predicts that any deviations from standard gravity emerge dynamically during structure formation rather than being imposed at early times. This ensures compatibility with early-universe constraints while leaving open the possibility of distinctive signatures in the nonlinear, late-time regime.

A full cosmological implementation is beyond the scope of the present work, but the construction presented here is consistent with standard cosmological behavior in the appropriate limits.

20 Discussion and Outlook

The results presented here demonstrate that galaxy rotation curves can be described by a simple, universal dynamical response mapping between baryonic and observed acceleration, without

invoking halo-specific tuning or galaxy-dependent parameters. Across a heterogeneous subset of SPARC rotation curves, the response framework reproduces the observed radial-acceleration relation with scatter comparable to established modified-gravity benchmarks, while exhibiting structured and predictive residual behaviour.

Three diagnostic outcomes are particularly noteworthy. First, the response law remains approximately universal under physically motivated splits (gas-dominated versus star-dominated systems, and low- versus high-surface- brightness proxies), supporting the interpretation of the response as a property of the gravitational medium rather than of individual galaxies. Second, allowing for mild nonlocality in the response does not lead to a statistically significant reduction in scatter relative to purely algebraic mappings on the present dataset, indicating that the data do not require explicit nonlocality at this level. Third, and most importantly, residuals are not randomly distributed but cluster in identifiable dynamical regimes, primarily at small radii and intermediate-to-low acceleration ratios.

This residual localisation distinguishes the present framework from purely algebraic interpolation laws. A model whose failures are structured and predictive is fundamentally more falsifiable than one whose deviations are distributed uniformly across parameter space. In this sense, the response approach does not merely fit the data but provides guidance on where and why it is expected to break down, highlighting specific targets for improved baryonic modelling and independent observational checks.

Several important extensions naturally follow from this work. The first is a fully dynamical treatment of environmental effects, in which the response depends explicitly on the time-dependent external gravitational field rather than on heuristic suppression prescriptions. The second is the possibility of temporal response or hysteresis, whereby the effective mapping depends on the evolutionary history of the baryonic potential rather than solely on its instantaneous configuration. The third is the requirement of cosmological consistency, including the emergence of the response scale in an expanding background and its compatibility with large-scale structure and lensing constraints.

These extensions are not required to interpret the present results, but they provide clear and testable directions for future work. The framework presented here establishes a minimal empirical baseline: any viable dynamical or medium-based theory of gravity must reproduce the observed response structure, its universality, and its predictive failure modes.

21 Discussion: Clarifications and Resolutions Provided by Paper I.5

This paper clarified several conceptual objections commonly raised against medium-based descriptions of gravity. Interpreting superfluid medium flow as phase-coherent motion resolves apparent energy-accumulation concerns and permits steady gravitational configurations without dissipation. Inertia emerges as resistance to reconfiguration under acceleration, while uniform motion corresponds to a stable co-moving state. Local Lorentz invariance is recovered as an emergent low-energy symmetry of excitations, consistent with existing experimental bounds. Illustrative simulations show that galaxy-scale regularities such as flat rotation curves and BTFR-like scaling can arise naturally from baryon-coupled medium response, providing concrete support for claims made in Paper I.

22 Conclusion and Outlook

This companion paper provided mechanistic clarification and supporting analysis for the unified ECSM cosmology introduced in Paper I. We clarified the meaning of "flow" as phase-coherent motion, outlined steady-state energy accounting, grounded inertia in resistance to medium

reconfiguration, and explained why local relativistic behavior can emerge effectively at low energies.

The simulations presented here are intended as qualitative demonstrations rather than precision fits. Detailed modeling of cosmological redshift, large-scale velocity fields (including Local Group motion and Virgo infall), and full cosmological parameter inference are deferred to subsequent work. With the foundational objections addressed, the framework is positioned for more detailed observational tests.